Blind Image Decomposition

Junlin Han[1,2] Weihao Li[1] Pengfei Fang[1,2] Chunyi Sun[2] Jie Hong[1,2]
Mohammad Ali Armin[1] Lars Petersson[1] Hongdong Li[2]

Data61-CSIRO[1]   Australian National University[2]

Abstract. We propose and study a novel task named **B**lind **I**mage **D**ecomposition (BID), which requires separating a superimposed image into constituent underlying images in a blind setting, that is, both the source components involved in mixing as well as the mixing mechanism are unknown. For example, rain may consist of multiple components, such as rain streaks, raindrops, snow, and haze. Rainy images can be treated as an arbitrary combination of these components, some of them or all of them. How to decompose superimposed images, like rainy images, into distinct source components is a crucial step toward real-world vision systems. To facilitate research on this new task, we construct multiple benchmark datasets, including mixed image decomposition across multiple domains, real-scenario deraining, and joint shadow/reflection/watermark removal. Moreover, we propose a simple yet general **B**lind **I**mage **De**composition **N**etwork (BIDeN) to serve as a strong baseline for future work. Experimental results demonstrate the tenability of our benchmarks and the effectiveness of BIDeN.
Codes and datasets are available at GitHub.

Keywords: Image Decomposition, Low-level Vision, Rain Removal

1   Introduction

Various computer vision and computer graphics tasks [23,99,41,45,27,38,29,2,15,1] can be viewed as image decomposition, which aims to separate a superimposed image into distinct components/layers with only a single observation. For example, foreground-background segmentation [16,70,51,3,53] aims at decomposing a holistic image into foreground objects and background stuff. Image dehazing [32,5,48] can be treated as decomposing a hazy image into a haze-free image and a haze map (medium transmission map, atmosphere light). Shadow removal [45,13,18,39,8,39] decomposes a shadow image into a shadow-free image and a shadow mask. Other tasks like transparency separation [92,17,47,57], watermark removal [54,7], image deraining [66,83,87,96,52,80], texture separation [27], underwater image restoration [22,30], image desnowing [56,69], stereo mixture decomposition [93], 3D intrinsic mixture image decomposition [2], fence removal [14,81,55], flare removal [79,4] are covered in image decomposition.

Vanilla image decomposition tasks come with a fixed and known number of source components, and the number is most often set to two [23,99,41,45,27,87,44].

(1) rs   (2) rs + snow   (3) rs + light haze

(4) rs + heavy haze   (5) rs + mh + raindrop   (6) rs + snow + mh + raindrop

rs: rain streak, mh: moderate haze
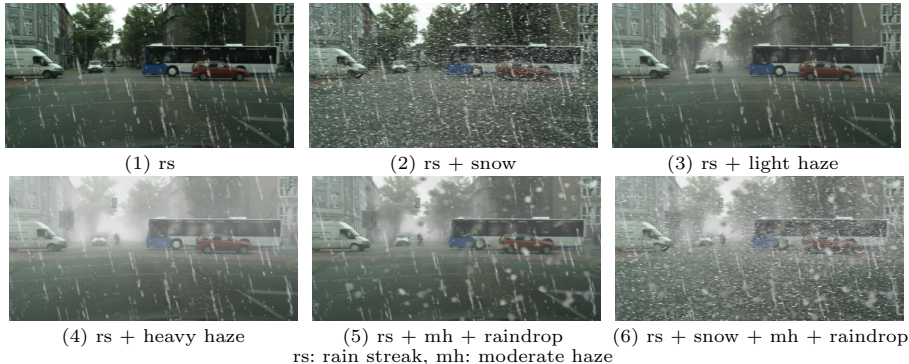
Fig. 1. Example of raining cases. Rain exists in different formats such as rain streak and raindrop. Snow and haze often co-occur during raining. BID setting treats rainy images as an arbitrary combination of these components. Deraining under the BID setting becomes more challenging yet more overarching

Such a setting does capture some basic real-world cases. However, real-world scenarios are more complex. Consider autonomous driving on rainy days, where the visual perception quality is degraded by different forms of precipitation and the co-occurring components, shown in Figure 1. Some natural questions emerge: Can a vision system assume precipitations to be of a specific form? Should a vision system assume raindrops always exist or not? Shall a vision system assume the haze or snow comes along with rain or not? These questions are particularly important based on their relevance in real-world applications. The answer to these questions should be *NO*. A comprehensive vision system is supposed to be robust with the ability to handle many possible circumstances [62,73,49]. Yet, with the previous setting in deraining [90,94,66,83,50,52,89,68,58,95,91,88] there remains a gap toward sophisticated real-world scenarios.

This paper aims at addressing the aforementioned gap, as a step toward robust real-world vision systems. We propose a task that: (1) does not fix the number of source components, (2) considers the presence and varying intensities of source components, and (3) amalgamates every source component as potential combinations. To disambiguate with previous tasks, we refer to our proposed task as *Blind Image Decomposition (BID)*. This name is inspired by the Blind Source Separation (BSS) task in the field of signal processing.

The task format is straightforward. We no longer set the number of source components to a fixed value. Instead, we set a maximum number of potential source components, where each component can be arbitrarily part of the mix. Let 'A', 'B', 'C', 'D', 'E' denote five source components and 'a', 'b', 'c', 'd', 'e' denote images from the corresponding source components. The mixed image can be either 'a', 'd', 'ab', 'bc', 'abd', 'ade', 'acde', 'abcde' · · ·, with up to 31 possible combinations in total. Given any of the 31 possible combinations as input, a BID method is required to predict and reconstruct the individual source components involved in mixing.

As different components can be arbitrarily involved in the mixing, no existing datasets support such a training protocol. Thus, we construct three benchmark datasets, they are: (I) mixed image decomposition across multiple domains, (II) real-scenario deraining, and (III) joint shadow/reflection/watermark removal.

To perform multiple BID tasks, we design a simple yet flexible model, dubbed BIDeN (Blind Image Decomposition Network). BIDeN is a generic model that supports diverse BID tasks with distinct objectives. BIDeN is based on the framework of GANs (Generative Adversarial Networks) [26], and we explore some critical design choices of BIDeN to present a general model. Designed for a more challenging BID setting, BIDeN still outperforms the current state-of-the-art image decomposition model [99,23] and shows competitive results compared to models designed for specific tasks. Lastly, a comprehensive ablation study is conducted to analyze the design choices of BIDeN.

2   Related Work

Image Decomposition. This task is a general task covering numerous computer vision and computer graphics tasks. Double-DIP [23] couples multiple DIPs [75] to decompose images into their basic components in an unsupervised manner. Deep Generative Priors [38] employs a likelihood-based generative model as a prior, performing the image decomposition task. Deep Adversarial Decomposition (DAD) [99] proposed a unified framework for image decomposition by employing three discriminators. A crossroad L1 loss is introduced to support pixel-wise supervision when domain information is unknown. Different from the conventional image decomposition task that usually aims to solve a particular degradation, in the BID setting, we treat degraded images as an arbitrary combination of individual components, and aim to solve sophisticated compound degradation in a unified framework.

Blind Source Separation. BSS [36,9,20,21,35], also known as the "cocktail party problem", is an important research topic in the field of signal processing. Blind refers to a setting where sources and mixing mechanism are both unknown. The task requires performing the separation of a mixture signal into the constituent underlying source signals with limited prior information. A representative algorithm is the Independent Component Analysis (ICA) [36,46,64]. The BID task shares common properties with BSS, where the blind settings are similar but not identical. The setting of BID assumes an unknown number of source components involved in the mixing and unknown mixing mechanisms. With such a setting, the number of source components involved in mixing is also unknown. However, the domain information of each source component is considered known as the goal of BID is to advance real-world vision systems. The setting of including known domain information can be better applied to computer vision tasks. For instance, the goal of the shadow removal task is to separate a shadow image into a shadow-free image and a shadow mask, where the domain information is clear.
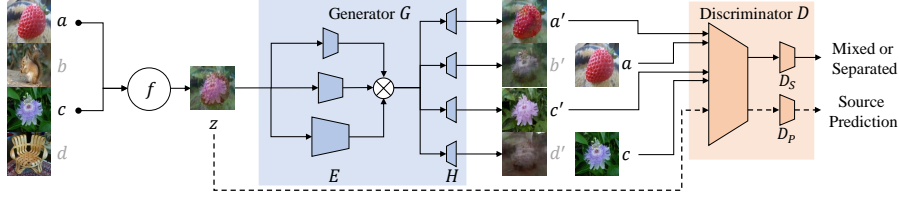
Fig. 2. The architecture of the Blind Image Decomposition Network (BIDeN). We show an example, where $N = 4$, $L = 2$, $x = \{a, b, c, d\}$, and $I = \{1, 3\}$. a, c are selected then passed to the mixing function f, and outputs the mixed input image z, which is $f(a, c)$ here. The generator consists of an encoder E with three branches and multiple heads H. $\bigotimes$ denotes the concatenation operation. Depth and receptive field of each branch are different to capture multiple scales of features. Each specified head points to the corresponding source component, and the number of heads varies with the maximum number of source components N. All reconstructed images (a', c') and their corresponding real images (a, c) are sent to an unconditional discriminator. The discriminator also predicts the source components involved in the mixing of the input image z. The outputs from other heads (b', d') do not contribute to the optimization

Generative Adversarial Networks. GANs [26] include two key components, a generator, and a discriminator, where the generator is trying to generate realistic samples while the discriminator is trying to identify real samples and generated samples. The adversarial training mechanism helps the output from the generator match the distribution of real data. GANs are especially successful in image generation tasks [86,42] and image-to-image translation tasks [37,31,98]. GANs are also a common tool for image decomposition tasks, where GANs have been successfully employed in image deraining [87,66], transparency separation [57,92], and image dehazing [48].

3 Blind Image Decomposition Formulation

Given a set of N ($N \geq 2$) source components, *i.e.*, image domains, denoted by $\mathcal{X} = \{X_m\}_{m=1}^N$. Each source component X_m contains some images x_m, $x_m \in X_m$. L ($1 \leq L \leq N$) source components are randomly selected from $\mathcal{X}$. Let $I = \{I_j\}_{j=1}^L$ indicate the index set for the selected source components, where $I_j \in \{1, ..., N\}$. Hence, the selected source components are denoted by $\{X_{I_j}\}_{j=1}^L$. Each selected source component X_{I_j} contains some images x_{I_j}. With a predetermined mixing function f, the mixed image z is given by $z = f(\{x_{I_j}\}_{j=1}^L)$. The mixed image z can be identical to a single image when $L = 1$. The BID task requires the BID method to find a function g to separate z, as $g(z) = \{x'_{I_j}\}_{j=1}^L$. Each reconstructed image x'_{I_j} is close to its corresponding image x_{I_j}. That is, given a mixed image as input, the task requires the BID method to: (1) predict the source components involved in mixing, (2) reconstruct images preserving the fidelity of the corresponding images involved in mixing.

For the example shown in Figure 2, where $N = 4$, $\mathcal{X} = \{A, B, C, D\}$, $x = \{a, b, c, d\}$, L can be $1, 2, 3, 4$, z can be $a, b, c, d, f(a,b), f(a,c), f(a,d), f(b,c), f(b,d), f(c,d), f(a,b,c), f(a,b,d), f(a,c,d), f(b,c,d), f(a,b,c,d)$. Let $L = 2$ and $I = \{1, 3\}$. Given $z = f(a,c)$ as the input, knowing there are four different source components A, B, C, D without any other information, the task requires the method to find a function g, so that $g(f(a,c)) = a', c'$, where $a' \to a$ and $c' \to c$. Also, the method should correctly predict the source components involved in the mixing, that is, predicting $I = \{1, 3\}$.

The BID task is challenging for the following reasons: (1) When N increases, the number of possible z increases rapidly. The BID setting forces the method to deal with $2^N - 1$ possible combinations. For instance, when N increases to 8, there are 255 variants of z. (2) The task requires the method to predict the source components involved in the mixing. Source components are difficult to be predicted when N is large and L varies a lot. (3) The mixing mechanism, or the mixing function f, is unknown to the method. The mixing function f varies with different source components and can be non-linear/complex in specific circumstances, such as rendering raindrop images, adding shadows or reflections to images. (4) As L increases, each source component contributes a decreasing amount of information to z, making the task highly ill-posed.

4   Blind Image Decomposition Network

To perform diverse BID tasks, a unified framework is required. Inspired by the success of image-to-image translation models [37,31,98], we design our Blind Image Decomposition Network (BIDeN) as follows. Figure 2 presents an overall architecture of BIDeN when the maximum number of source components is four.

The generator G consists of two parts: a multi-scale encoder E and multiple heads H. We design a multi-scale encoder containing three branches to capture multiple scales of features. This design is beneficial to the reconstruction of source components. We concatenate different scales of features and send them to multiple heads, where the number of heads is identical to the maximum number of source components. Each head is specific to reconstructing a particular kind of source component. Such multiple-head domain-specific autoencoders have been adopted particularly in inverse rendering task [29,78].

The discriminator D consists of two branches and most weights are shared. The reconstructed images and corresponding real images are sent to the discriminator branch D_S (Separation) individually. The function of D_S is similar to a typical discriminator, *i.e.*, classifying whether the input to D_S is generated or real to direct the generator generating realistic images. The discriminator branch D_P (Prediction) predicts the source components involved in the mixed image z, with a confidence threshold of zero. A successful prediction unveils the correct index set of the selected source components I.

Taking the example of Figure 2, we name four heads as H_A, H_B, H_C, and H_D. For an input $f(a,c)$, H_A and H_C aim to reconstruct a', c', so that $a' \to a$ and $c' \to c$ while H_B, H_D are free to output anything or are simply turned

off. We employ adversarial loss [26], perceptual loss [40], L1/L2 loss, and binary cross-entropy loss. The details of the objective function are expressed below.

4.1 Objective

We employ the adversarial loss [26] to encourage the generator G to output well separated and realistic images, regardless of the source components. For the function $g(z) = \{x'_{I_j}\}_{j=1}^{L}$, the GAN loss is expressed as:

$$\mathcal{L}_{\mathrm{GAN}}(G, D_S) = \mathbb{E}_x\left[\log D_S(x)\right] \\ + \mathbb{E}_z\left[\log\left(1 - D_S(G(z))\right)\right], \tag{1}$$

where G behaves as g. It tries to separate the input mixed image z and reconstruct separated outputs x'_{I_j}, while D_S attempts to distinguish between $G(z)$ and real samples x_{I_j}. Note x inside equations 1-5 denotes x_{I_j}. We employ the LSGAN [59] loss and the Markovian discriminator [37].

The reconstructed images x'_{I_j} should be separated, as well as to be near the corresponding x_{I_j} in a distance sense. Hence, we employ perceptual loss (VGG loss) [40] and L1/L2 loss. They are formalized as:

$$\mathcal{L}_{\mathrm{VGG}}(G) = \mathbb{E}_{x,z}[\sum_l \lambda_l\left[\|\Phi_l(x) - \Phi_l(G(z)))\|_1\right], \tag{2}$$

$$\mathcal{L}_{\mathrm{L1}}(G) = \mathbb{E}_{x,z}\left[\|x - G(z)\|_1\right], \tag{3}$$

$$\mathcal{L}_{\mathrm{L2}}(G) = \mathbb{E}_{x,z}\left[\|x - G(z)\|_2^2\right], \tag{4}$$

where Φ is a trained VGG19 [72] network, Φ_l denotes a specific layer, and λ_l denotes the weights for the l-th layer. The choice of layers and weights is identical to pix2pixHD [77]. We use L2 loss for masks and L1 loss for other source components. For simplification, we denote L1/L2 loss as $\mathcal{L}_{\mathrm{L}}$.

For the source prediction task, we find that the discriminator performs better than the generator. The goal of the discriminator is to classify between reconstructed samples and real samples. It naturally learns an embedding. Such an embedding is beneficial even when the input is a mixed image z. The discriminator D is capable of performing an additional source prediction task. Thus we design a source prediction branch D_P. The binary cross-entropy loss is employed for the source prediction task:

$$\mathcal{L}_{\mathrm{BCE}}(D_P) = \mathbb{E}_z[-\sum_{m=1}^{N}[GT(z)_m \log(D_P(z)_m) \\ + (1 - GT(z)_m)\log(1 - D_P(z)_m)]], \tag{5}$$

where N denotes the maximum number of source components, GT denotes the binary label of the source components involved in the mixing of input image z. D_P is the source prediction branch of the discriminator.

Our final objective function is:

$$
\begin{aligned}
\mathcal{L}(G, D_S, D_P) = & \lambda_{\mathrm{GAN}} \mathcal{L}_{\mathrm{GAN}}\left(G, D_S\right) + \lambda_{\mathrm{VGG}} \mathcal{L}_{\mathrm{VGG}}(G) \\
& + \lambda_{\mathrm{L}} \mathcal{L}_{\mathrm{L}}(G) + \lambda_{\mathrm{BCE}} \mathcal{L}_{\mathrm{BCE}}(D_P).
\end{aligned}
\tag{6}
$$

We set $\lambda_{\mathrm{GAN}}, \lambda_{\mathrm{VGG}}, \lambda_{\mathrm{L}}, \lambda_{\mathrm{BCE}}$ to be 1, 10, 30, 1 respectively. This setting is a generic setting that is applied to all tasks.

4.2   Training details

Throughout all experiments, we use the Adam optimizer [43] with $\beta_1 = 0.5$ and $\beta_2 = 0.999$ for both G, D. BIDeN is trained for 200 epochs with a learning rate of 0.0003. The learning rate starts to decay linearly after half of the total epochs. We use a batch size of 1 and instance normalization [74]. All training images are loaded as 286×286 then cropped to 256×256 patches. Horizontal flip is randomly applied. At test time, we load test images in a 256×256 resolution. More details on the training settings, the architecture, the number of parameters, and training speed are provided in the Appendix A. The training details of all baselines are also provided there.

5   Blind Image Decomposition Tasks

We construct benchmark datasets from different views to support practical usages of BID. For each benchmark dataset, we involve multiple source components that may occur together. To explore the generality of BIDeN and the tenability of constructed datasets, we test BIDeN on three new challenging datasets. BIDeN is trained under the BID setting, which is more difficult than the conventional image decomposition setting. During training, mixed images are randomly synthesized. At test time, the input mixed images are fixed. As BID is a novel task not previously investigated, no existing baselines are available for comparison. For different tasks, we choose different evaluation strategies and baselines.

Throughout all tasks, BIDeN is trained under the BID setting, that is, BIDeN is facing more challenging requirements than other baselines. Also, BIDeN is a generic model designed to perform all kinds of BID tasks. These two constraints limit the performance of BIDeN. We compare BIDeN to other baselines designed for specific tasks, where BIDeN is still able to show very competitive results on all tasks. All qualitative results are ***randomly picked***. Additional task settings, discussion on the order of mixing, dataset construction details, results, including the detailed case results of BIDeN, are provided in the Appendix A.3.

5.1   Task I: Mixed image decomposition across multiple domains

Dataset. This dataset contains eight different image domains, *i.e.*, source components. Each domain has approximately 2500 to 3000 images in the training set, and the test set contains 300 images for each domain. Image domains are
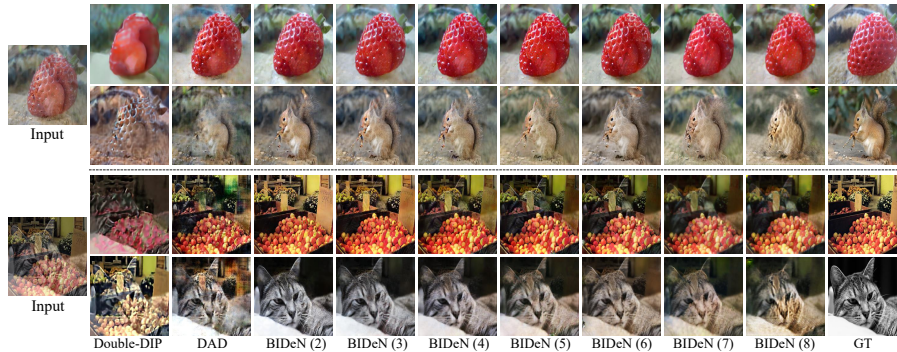
Fig. 3. Qualitative results of Task I (Mixed image decomposition across multiple domains). We train BIDeN 7 times, setting different maximum numbers of source components (2-8). Double-DIP fails to separate the mixed input. DAD shows blurry, non-clean results while the results shown by BIDeN are well-separated and visually satisfying. When BIDeN is trained on a greater maximum number of source components, the quality of the results drops progressively as expected

designed to be big and inclusive to cover multiple categories, like animal, fruit, vehicle, instead of being comparatively small domains such as horse, cat, car. The eight domains are Fruit (2653), Animal (2653), Flower (2950), Furniture (2582), Yosemite (2855), Vehicle (2670), Vegetable (2595), and CityScape (2975). CityScape and Flower are selected from the CityScape [11] dataset and the VGG flower [63] dataset. The remaining six image domains are mainly gathered from Flicker using the corresponding keyword, except for Yosemite, which also combines the Summer2Winter dataset from CycleGAN [98]. The order of the eight domains is randomly shuffled. The mixing mechanism is linear mix.

Table 1. Quantitative results on Task I (Mixed image decomposition across multiple domains). The testing condition is identical, using Fruit (A) + Animal (B) mixture as inputs. N in BIDeN (N) denotes the maximum number of source components. Double-DIP [23] performs poorly. Under a more challenging BID setting, BIDeN (2,3,4) still outperforms DAD [99] overall, suggesting the superiority of BIDeN. Please refer to Appendices for detailed case results

Method	Fruit (A)			Animal (B)			Acc (AB) ↑	Acc (All) ↑	Model size
	PSNR↑	SSIM↑	FID↓	PSNR↑	SSIM↑	FID↓			
Double-DIP [23]	13.14	0.49	257.80	13.11	0.39	221.76	-	-	-
DAD [99]	17.59	0.72	137.66	17.52	0.62	126.32	0.996	-	669.0 MB
BIDeN (2)	20.07	0.79	62.99	19.89	0.69	69.35	1.0	0.957	144.9 MB
BIDeN (3)	19.04	0.75	74.68	18.75	0.61	88.23	0.836	0.807	147.1 MB
BIDeN (4)	18.19	0.73	79.03	18.03	0.58	97.16	0.716	0.733	149.3 MB
BIDeN (5)	17.66	0.71	81.17	17.27	0.54	114.40	0.676	0.603	151.5 MB
BIDeN (6)	17.28	0.69	85.64	16.57	0.51	118.00	0.646	0.483	153.7 MB
BIDeN (7)	16.70	0.68	97.26	16.54	0.49	126.66	0.413	0.310	155.9 MB
BIDeN (8)	16.49	0.67	105.61	15.79	0.45	191.29	0.383	0.278	158.1 MB

Experiments and results. We compare BIDeN to Double-DIP [23] and DAD [99]. DAD is trained on the first two domains (Fruit, Animal) with mixed input only. For BIDeN, we train it 7 times under the BID setting, varying from 2 domains to 8 domains. At test time, we evaluate the separation results on Fruit + Animal mixture withPSNR, SSIM [97], and FID [33].

Table 1 and Figure 3 present the results of Task I. In terms of PSNR/SSIM, BIDeN outperforms Double-DIP by a large margin and outperforms DAD when N is less than 5. For FID, BIDeN shows preferable results than DAD even when $N = 7$, showing the superiority of BIDeN.

5.2   Task II: Real-scenario deraining

We design two sub-tasks, real-scenario deraining in driving (Task II.A) and real-scenario deraining in general (Task II.B).

Task II.A: Real scenario deraining in driving

Dataset. Based on the CityScape [11] dataset, we construct our real-scenario deraining in driving dataset. We use the test set from the original CityScape dataset as our training set (2975), and the validation set from the original CityScape dataset as our test set (500). The test set for all source components contains a fixed number of 500 images. We use three different masks, including rain streak (1620), raindrop (3500), and snow (3500). These masks cover different intensities. For haze, we use the corresponding transmission maps (2975 x 3) with three different intensities acquired from Foggy CityScape [71]. The masks for rain streak are acquired from Rain100L and Rain100H [83] while the masks for snow are selected from Snow100K [56]. For raindrop masks, we model the droplet shape and property using the metaball model [6]. The locations, numbers, and sizes of raindrops are randomly sampled. Paired refraction maps are generated using refractive model [10,65]. The mixing mechanism for this dataset is based on physical imaging models [83,56,32,10,65].
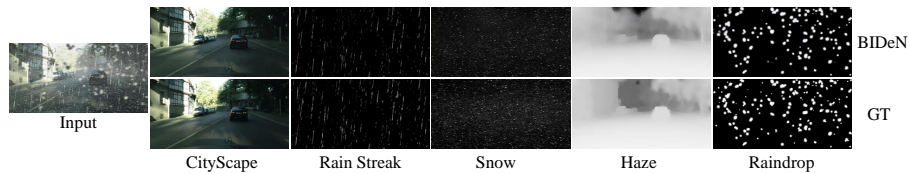
Fig. 4. CityScape, masks (Rain Streak, Snow, Raindrop), and transmission map (Haze) generated by BIDeN for case (6), rain streak + snow + moderate haze + raindrop. All generated images are perceptually faithful and visually close to the ground truth (GT)

Experiments and results. We train BIDeN, MPRNet [85], Restormer [84], and RCDNet [76] under the BID setting. For all baselines, we do not require the prediction of the source component and the generation of masks. Thus, BIDeN is still trained with a more challenging requirement. We report the results for 6

Table 2. Results of BIDeN on Task II.A (Real-scenario deraining in driving). We employ PSNR and SSIM metrics for both CityScape images, masks, and transmission maps. We report the results for 6 test cases as presented in Figure 1, the 6 cases are (1): rain streak, (2): rain streak + snow, (3): rain streak + light haze, (4): rain streak + heavy haze, (5): rain streak + moderate haze + raindrop, (6) rain streak + snow + moderate haze + raindrop. Note that only haze is divided into light/moderate/heavy intensities. Both training set and test set of Rain Streak, Snow, and Raindrop already consist of different intensities

Method	CityScape		Rain Streak		Snow		Haze		Raindrop		Acc ↑
	PSNR↑	SSIM↑	PSNR↑	SSIM↑	PSNR↑	SSIM↑	PSNR↑	SSIM↑	PSNR↑	SSIM↑	
BIDeN (1)	30.89	0.932	32.13	0.924	-	-	-	-	-	-	0.998
BIDeN (2)	29.34	0.899	29.24	0.846	25.77	0.692	-	-	-	-	0.996
BIDeN (3)	28.62	0.919	31.48	0.914	-	-	30.77	0.960	-	-	0.994
BIDeN (4)	26.77	0.898	30.57	0.897	-	-	33.73	0.957	-	-	0.998
BIDeN (5)	27.11	0.898	30.54	0.898	-	-	30.52	0.952	20.20	0.908	0.994
BIDeN (6)	26.44	0.870	28.31	0.823	24.79	0.658	29.83	0.948	21.47	0.893	0.998

cases, as the examples presented in Figure 1. Note that only haze is divided into light/moderate/heavy intensities. Both training set and test set of rain streak, snow, and raindrop already contain different intensities. We report the results in SSIM and PSNR for CityScape images, masks, and transmission maps.   For

| Input | MPRNet | Restormer | RCDNet | BIDeN | GT |

Fig. 5. Results of Task II.A (Real-scenario deraining in driving). Row 1-6 presents 6 cases as presented in Table 2. Baselines performs well at case (1) and they effectively removes rain streak but is not strong at removing other components. BIDeN is more robust at the removal of all components. BIDeN generates artifact-free, visually pleasing results while all baselines leaves some components that are not completely removed, especially when hazy intensity is moderate or heavy, as shown in case (4), (5), and (6)

all 6 cases, we report the detailed results of BIDeN in Table 2. BIDeN shows excellent quantitative results on accuracy. For the PSNR/SSIM metrics on all source components, BIDeN performs well except for the raindrop masks. An

Table 3. Comparison on task II.A (Real-scenario deraining in driving) between MPR-Net [85], RCDNet [76], and BIDeN. MPRNet and Rostormer shows superior results for case (1) and case (2). In contrast, BIDeN is better at other cases. For the details of 6 test cases, please refer to Table 2 and Figure 1

Case	Input		MPRNet		Restormer		RCDNet		BIDeN	
	PSNR↑	SSIM↑	PSNR↑	SSIM↑	PSNR↑	SSIM↑	PSNR↑	SSIM↑	PSNR↑	SSIM↑
(1)	25.69	0.786	33.39	0.945	34.29	0.951	32.38	0.937	30.89	0.932
(2)	18.64	0.564	30.52	0.909	30.60	0.917	28.45	0.892	29.34	0.899
(3)	17.45	0.712	23.98	0.900	23.74	0.905	27.14	0.911	28.62	0.919
(4)	11.12	0.571	18.54	0.829	20.33	0.853	19.67	0.865	26.77	0.898
(5)	14.05	0.616	21.18	0.846	22.17	0.859	24.23	0.889	27.11	0.898
(6)	12.38	0.461	20.76	0.812	21.24	0.821	22.93	0.846	26.44	0.870

example of all components generated by BIDeN is shown in Figure 4. Table 3 and Figure 5 presents the comparison between BIDeN and baselines. For better visualization, we resize the resolution of visual examples to match the original CityScape resolution.

Task II.B: Real scenario deraining in general

Dataset. The training set contains 3661 natural images as rain-free images, where 861 images are adopted from the training set of [66], 1800 images are borrowed from the training set of Rain1800 [83], and the rest 1000 images are selected from the training set of Snow100K [56]. We adopt identical rain streak, snow, and raindrop masks from Task II.A. The test set contains real images only, including rain streak (185, from [50]), raindrop (249, from [66]) and snow (1329, from [56]) images.

Table 4. Quantitative results of Task II.B (Real-scenario deraining in general). * indicates the BID setting. For all methods and testing cases, models trained under the BID setting performs better than the conventional image decomposition setting

Method	Rain Streak		Raindrop		Snow	
	NIQE↓	BRISQUE↓	NIQE↓	BRISQUE↓	NIQE↓	BRISQUE↓
Input	4.86	27.84	5.61	24.85	4.74	22.68
MPRNet	4.14	28.72	4.94	29.42	4.60	25.93
MPRNet*	4.34	28.00	4.81	25.86	4.24	24.55
BIDeN	4.71	25.39	5.39	22.94	4.97	22.64
BIDeN*	4.31	26.55	4.71	21.22	4.28	22.40

Experiments and results. We aim to validate whether models trained on the synthetic dataset can generalize to real testing samples and whether the BID training setting generalizes better than the conventional image decomposition setting. We train BIDeN and MPRNet under the BID setting as well as the conventional image decomposition setting with identical training recipes, that is, the training recipes used in Task II.A. For the conventional image decomposition setting, models are trained on a large-scale synthetic dataset [85] (13712 pairs). We report the quantitative results with no-reference metrics, NIQE [61] and BRISQUE [60].

| Input | MPRNet | MPRNet* | BIDeN | BIDeN* | BIDeN* mask |
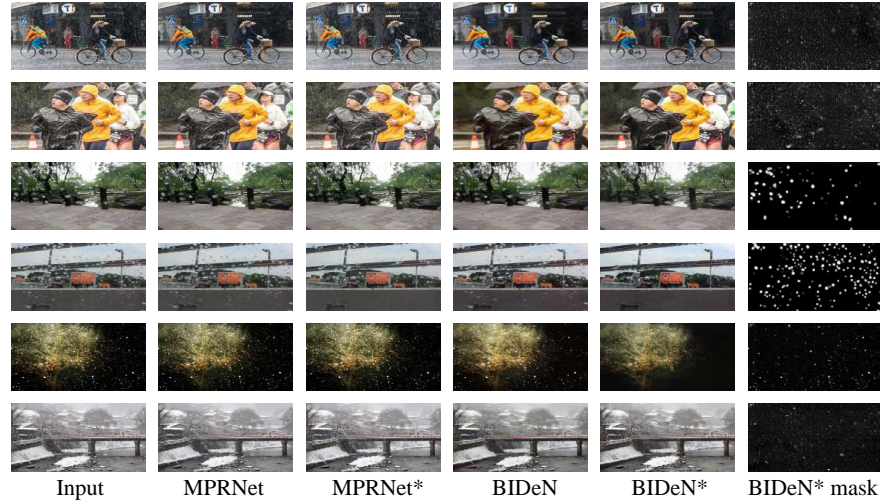
Fig. 6. Qualitative results of Task II.B (Real-scenario deraining in general). * indicates the BID setting. Rows 1-2, 3-4, and 5-6 presents the results of real rain streak, raindrop, and snow images, respectively. For all cases, models trained under the BID setting are more robust in restoring real-world images

All trained models are evaluated with real-world images. Results are presented in Table 4 and Figure 6. With only 26.6% training data and iterations, both BIDeN and MPRNet models trained under the BID setting are more robust in restoring real images, showing the generality and robustness of the BID setting in real-world scenarios.

5.3   Task III: Joint shadow/reflection/watermark removal
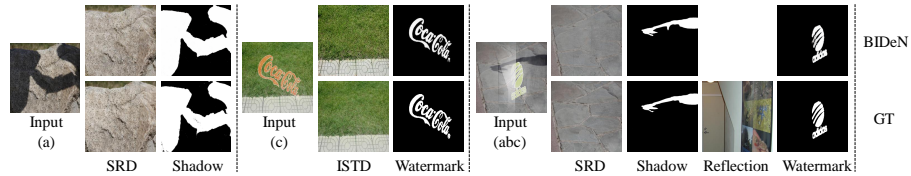
**Fig. 7.** Images and masks (Shadow, Watermark) produced by BIDeN for three cases, (a), (c), and (abc). All generated masks are faithful to the ground truth (GT)

Dataset. This task is designed to jointly perform multiple tasks with uncertainty in one go. Once a model is trained on this dataset under the BID setting, the model is capable of performing multiple tasks. We construct two versions for this

Table 5. Results of Task III (Joint shadow/reflection/watermark removal). We employ RMSE↓ to measure shadow region, non-shadow region, and all region. For BIDeN, we report the performance of all cases. a,b,c denotes shadow, reflection, and watermark, respectively. BIDeN (ab) is the result of BIDeN tested on shadow + reflection inputs. Results for all baselines are reported by [12,19]. The generality of BIDeN and the challenging BID training setting limit the performance of BIDeN

Method	Version one (V1), ISTD				Version two (V2), SRD			
	Shadow	Non-Shadow	All	Acc	Shadow	Non-Shadow	All	Acc
Bilateral [82]	19.82	14.83	15.63	-	23.43	22.26	22.57	-
Regions [28]	18.95	7.46	9.30	-	29.89	6.47	12.60	-
Interactive [25]	14.98	7.29	8.53	-	19.58	4.92	8.73	-
DSC [34]	9.48	6.14	6.67	-	10.89	4.99	6.23	-
DHAN [12]	8.14	6.04	6.37	-	8.94	4.80	5.67	-
Auto-Exposure [19]	7.77	5.56	5.92	-	8.56	5.75	6.51	-
CANet [8]	8.86	6.07	6.15	-	7.82	5.88	5.98	-
BIDeN (a)	11.55	10.24	10.45	0.359	12.06	7.47	8.73	0.919
BIDeN (ab)	12.96	10.77	11.12	0.661	14.10	8.16	9.79	0.911
BIDeN (ac)	11.89	10.23	10.50	0.694	13.29	8.08	9.51	0.943
BIDeN (abc)	13.20	10.76	11.16	0.929	15.28	8.85	10.62	0.936
BIDeN (b)	-	-	10.85	0.559	-	-	8.01	0.891
BIDeN (c)	-	-	10.20	0.461	-	-	7.92	0.914
BIDeN (bc)	-	-	10.77	0.727	-	-	8.71	0.879

dataset, Version one (V1) is based on ISTD [77], and Version two (V2) is based on SRD [67,12]. We use paired shadow masks, shadow-free images, and shadow images from ISTD/SRD. ISTD consists of 1330 training images and 540 test images while SRD contains 2680 training images and 408 testing images. The algorithm for adding reflection to images is acquired from [92], we select 3120 images from the reflection subset [92] as the reflection layer. The watermark generation algorithm as well as the paired watermark masks, RGB watermark images are acquired from LVM [54], we select 3000 paired watermark images and masks from the training set of LVW [54].

Following the data split of ISTD and SRD, both V1 and V2 share 2580 reflection layer images and 2460 watermark images/masks. V1 contains 1330 paired shadow-free images/shadow masks and the test set contains 540 images for every source component. V2 includes 2680 paired shadow-free images/shadow masks and the test set contains 408 images for every source component. Note that we do not require the reconstruction of reflection layer images.

Experiments and results. We mainly compare the shadow removal results to multiple shadow removal baselines, including [82,28,25,34,12,19,8]. We train BIDeN under the BID setting. The trained BIDeN is capable of dealing with all combinations between shadow/reflection/watermark removal tasks. At test time, we report the results for all cases. We employ the root mean square error (RMSE) in LAB color space, following [12,19].

The quantitative results for Task III are reported in Table 5. Constrained by the generality of BIDeN and the challenging BID training setting, BIDeN does not show superior quantitative results compared to other baselines designed for the shadow removal task only. Please refer to the Appendix B.3 for qualitative results.

6 Ablation Study and Analysis

We perform ablation experiments to analyze the effectiveness of each component inside BIDeN. Evaluation is performed on Task I (Mixed image decomposition across multiple domains). We set the maximum number of source components to be 4 throughout all ablation experiments. The results are shown in Table 6.

Ablation	Fruit (A) PSNR↑	Animal (B) PSNR↑	Acc (AB) ↑	Acc (All) ↑
I	17.26	17.05	0.730	0.732
II	17.95	17.41	0.566	0.616
III	16.67	16.34	0.706	0.722
IV	15.56	13.65	0.733	0.753
V	18.04	17.98	0.0	0.06
VI	18.19	17.97	0.634	0.698
VII	18.13	17.98	0.520	0.609
VIII	15.68	15.64	0.716	0.683
BIDeN	**18.19**	**18.03**	**0.716**	**0.733**

Table 6. Ablation study on the design choices of BIDeN. (I) Single-scale encoder. (II) No adversarial loss. (III) No perceptual loss. (IV) No L1/L2 loss. (V) No binary cross-entropy loss. (VI) Source prediction branch inside the generator. (VII) No weights sharing between two branches of discriminator. (VIII) Zeroed loss

Multi-scale encoder (I). We present the results of using a single-scale encoder to replace the multi-scale encoder. BIDeN yields better performance when the multi-scale encoder is employed, which validates the effectiveness of our design.
Choice of losses (II, III, IV, V). BIDeN consists of four different losses, we show that removing either one of the losses leads to a performance drop.
Source prediction branch (VI, VII). We move the prediction branch D_P to the generator. This change degrades the performance, showing that the source prediction task is better to be performed by the discriminator. We report the results for a variant where D_P does not share weights with the separation branch D_S. The performance of this variant is worse than vanilla BIDeN, indicating that the embedding learned by D_S is beneficial to D_P.
Zeroed loss (VIII). Taking the example of Figure 2, four heads are H_A, H_B, H_C, and H_D. By default, BIDeN ignores the outputs from H_B and H_D. Here, we encourage the outputs from H_B and H_D to be zero pixels. Such a zeroed loss forces the generator to perform the source prediction task implicitly, however, the results after applying zeroed loss are not comparable to default BIDeN.

7 Conclusion

We believe BID is a novel computer vision task advancing real-world vision systems. We form a solid foundation for the future study and we invite the community to further explore its potential, including discovering interesting areas of application, developing novel methods, extending the BID setting, and constructing benchmark datasets. We expect more application areas related to image decomposition, especially in image deraining, to apply the BID setting.

References

1. Alayrac, J.B., Carreira, J., Zisserman, A.: The visual centrifuge: Model-free layered video representations. In: Proceedings of the IEEE/CVF Conference on Computer Vision and Pattern Recognition. pp. 2457–2466 (2019)
2. Alhaija, H.A., Mustikovela, S.K., Thies, J., Jampani, V., Nießner, M., Geiger, A., Rother, C.: Intrinsic autoencoders for joint deferred neural rendering and intrinsic image decomposition. In: 2020 International Conference on 3D Vision (3DV). pp. 1176–1185. IEEE (2020)
3. Alpert, S., Galun, M., Brandt, A., Basri, R.: Image segmentation by probabilistic bottom-up aggregation and cue integration. IEEE transactions on pattern analysis and machine intelligence **34**(2), 315–327 (2011)
4. Asha, C., Bhat, S.K., Nayak, D., Bhat, C.: Auto removal of bright spot from images captured against flashing light source. In: 2019 IEEE International Conference on Distributed Computing, VLSI, Electrical Circuits and Robotics (DISCOVER). pp. 1–6. IEEE (2019)
5. Berman, D., Avidan, S., et al.: Non-local image dehazing. In: Proceedings of the IEEE conference on computer vision and pattern recognition. pp. 1674–1682 (2016)
6. Blinn, J.F.: A generalization of algebraic surface drawing. ACM transactions on graphics (TOG) **1**(3), 235–256 (1982)
7. Chen, X., Wang, W., Bender, C., Ding, Y., Jia, R., Li, B., Song, D.: Refit: a unified watermark removal framework for deep learning systems with limited data. In: Proceedings of the 2021 ACM Asia Conference on Computer and Communications Security. pp. 321–335 (2021)
8. Chen, Z., Long, C., Zhang, L., Xiao, C.: Canet: A context-aware network for shadow removal. In: ICCV. pp. 4743–4752 (2021)
9. Cichocki, A., Amari, S.i.: Adaptive blind signal and image processing: learning algorithms and applications. John Wiley & Sons (2002)
10. Cohen, J., Olano, M., Manocha, D.: Appearance-preserving simplification. In: Proceedings of the 25th annual conference on Computer graphics and interactive techniques. pp. 115–122 (1998)
11. Cordts, M., Omran, M., Ramos, S., Rehfeld, T., Enzweiler, M., Benenson, R., Franke, U., Roth, S., Schiele, B.: The cityscapes dataset for semantic urban scene understanding. In: Proceedings of the IEEE conference on computer vision and pattern recognition. pp. 3213–3223 (2016)
12. Cun, X., Pun, C.M., Shi, C.: Towards ghost-free shadow removal via dual hierarchical aggregation network and shadow matting gan. In: Proceedings of the AAAI Conference on Artificial Intelligence. vol. 34, pp. 10680–10687 (2020)
13. Ding, B., Long, C., Zhang, L., Xiao, C.: Argan: Attentive recurrent generative adversarial network for shadow detection and removal. In: Proceedings of the IEEE/CVF International Conference on Computer Vision. pp. 10213–10222 (2019)
14. Du, C., Kang, B., Xu, Z., Dai, J., Nguyen, T.: Accurate and efficient video defencing using convolutional neural networks and temporal information. In: 2018 IEEE International Conference on Multimedia and Expo (ICME). pp. 1–6. IEEE (2018)
15. Fadili, M.J., Starck, J.L., Bobin, J., Moudden, Y.: Image decomposition and separation using sparse representations: An overview. Proceedings of the IEEE **98**(6), 983–994 (2009)
16. Faktor, A., Irani, M.: Co-segmentation by composition. In: Proceedings of the IEEE international conference on computer vision. pp. 1297–1304 (2013)

17. Fan, Q., Yang, J., Hua, G., Chen, B., Wipf, D.: A generic deep architecture for single image reflection removal and image smoothing. In: Proceedings of the IEEE International Conference on Computer Vision. pp. 3238–3247 (2017)
18. Finlayson, G.D., Drew, M.S., Lu, C.: Entropy minimization for shadow removal. International Journal of Computer Vision **85**(1), 35–57 (2009)
19. Fu, L., Zhou, C., Guo, Q., Juefei-Xu, F., Yu, H., Feng, W., Liu, Y., Wang, S.: Auto-exposure fusion for single-image shadow removal. In: Proceedings of the IEEE/CVF Conference on Computer Vision and Pattern Recognition. pp. 10571–10580 (2021)
20. Gai, K., Shi, Z., Zhang, C.: Blindly separating mixtures of multiple layers with spatial shifts. In: 2008 IEEE Conference on Computer Vision and Pattern Recognition. pp. 1–8. IEEE (2008)
21. Gai, K., Shi, Z., Zhang, C.: Blind separation of superimposed images with unknown motions. In: 2009 IEEE Conference on Computer Vision and Pattern Recognition. pp. 1881–1888. IEEE (2009)
22. Galdran, A., Pardo, D., Picón, A., Alvarez-Gila, A.: Automatic red-channel underwater image restoration. Journal of Visual Communication and Image Representation **26**, 132–145 (2015)
23. Gandelsman, Y., Shocher, A., Irani, M.: ” double-dip”: Unsupervised image decomposition via coupled deep-image-priors. In: Proceedings of the IEEE/CVF Conference on Computer Vision and Pattern Recognition. pp. 11026–11035 (2019)
24. Glorot, X., Bengio, Y.: Understanding the difficulty of training deep feedforward neural networks. In: Proceedings of the thirteenth international conference on artificial intelligence and statistics. pp. 249–256 (2010)
25. Gong, H., Cosker, D.: Interactive shadow removal and ground truth for variable scene categories. In: BMVC. pp. 1–11. Citeseer (2014)
26. Goodfellow, I., Pouget-Abadie, J., Mirza, M., Xu, B., Warde-Farley, D., Ozair, S., Courville, A., Bengio, Y.: Generative adversarial nets. In: Advances in neural information processing systems (2014)
27. Gu, S., Meng, D., Zuo, W., Zhang, L.: Joint convolutional analysis and synthesis sparse representation for single image layer separation. In: Proceedings of the IEEE International Conference on Computer Vision. pp. 1708–1716 (2017)
28. Guo, R., Dai, Q., Hoiem, D.: Paired regions for shadow detection and removal. IEEE transactions on pattern analysis and machine intelligence **35**(12), 2956–2967 (2012)
29. Halperin, T., Ephrat, A., Hoshen, Y.: Neural separation of observed and unobserved distributions. In: International Conference on Machine Learning. pp. 2566–2575. PMLR (2019)
30. Han, J., Shoeiby, M., Malthus, T., Botha, E., Anstee, J., Anwar, S., Wei, R., Armin, M.A., Li, H., Petersson, L.: Underwater image restoration via contrastive learning and a real-world dataset. arXiv preprint arXiv:2106.10718 (2021)
31. Han, J., Shoeiby, M., Petersson, L., Armin, M.A.: Dual contrastive learning for unsupervised image-to-image translation. In: Proceedings of the IEEE/CVF Conference on Computer Vision and Pattern Recognition Workshops (2021)
32. He, K., Sun, J., Tang, X.: Single image haze removal using dark channel prior. IEEE transactions on pattern analysis and machine intelligence **33**(12), 2341–2353 (2010)
33. Heusel, M., Ramsauer, H., Unterthiner, T., Nessler, B., Hochreiter, S.: Gans trained by a two time-scale update rule converge to a local nash equilibrium. In: Advances in neural information processing systems (2017)

34. Hu, X., Fu, C.W., Zhu, L., Qin, J., Heng, P.A.: Direction-aware spatial context features for shadow detection and removal. IEEE transactions on pattern analysis and machine intelligence **42**(11), 2795–2808 (2019)
35. Hyvärinen, A., Oja, E.: A fast fixed-point algorithm for independent component analysis. Neural computation **9**(7), 1483–1492 (1997)
36. Hyvärinen, A., Oja, E.: Independent component analysis: algorithms and applications. Neural networks **13**(4-5), 411–430 (2000)
37. Isola, P., Zhu, J.Y., Zhou, T., Efros, A.A.: Image-to-image translation with conditional adversarial networks. In: Proceedings of the IEEE conference on computer vision and pattern recognition. pp. 1125–1134 (2017)
38. Jayaram, V., Thickstun, J.: Source separation with deep generative priors. In: International Conference on Machine Learning. pp. 4724–4735. PMLR (2020)
39. Jin, Y., Sharma, A., Tan, R.T.: Dc-shadownet: Single-image hard and soft shadow removal using unsupervised domain-classifier guided network. In: Proceedings of the IEEE/CVF International Conference on Computer Vision. pp. 5027–5036 (2021)
40. Johnson, J., Alahi, A., Fei-Fei, L.: Perceptual losses for real-time style transfer and super-resolution. In: European conference on computer vision. pp. 694–711. Springer (2016)
41. Kang, L.W., Lin, C.W., Fu, Y.H.: Automatic single-image-based rain streaks removal via image decomposition. IEEE transactions on image processing **21**(4), 1742–1755 (2011)
42. Karras, T., Laine, S., Aila, T.: A style-based generator architecture for generative adversarial networks. In: Proceedings of the IEEE/CVF Conference on Computer Vision and Pattern Recognition. pp. 4401–4410 (2019)
43. Kingma, D.P., Ba, J.: Adam: A method for stochastic optimization. International Conference on Learning Representations (ICLR) (2014)
44. Kong, Q., Xu, Y., Wang, W., Jackson, P.J., Plumbley, M.D.: Single-channel signal separation and deconvolution with generative adversarial networks. arXiv preprint arXiv:1906.07552 (2019)
45. Le, H., Samaras, D.: Shadow removal via shadow image decomposition. In: Proceedings of the IEEE/CVF International Conference on Computer Vision. pp. 8578–8587 (2019)
46. Lee, T.W., Lewicki, M.S., Sejnowski, T.J.: Ica mixture models for unsupervised classification of non-gaussian classes and automatic context switching in blind signal separation. IEEE Transactions on Pattern Analysis and Machine Intelligence **22**(10), 1078–1089 (2000)
47. Li, C., Yang, Y., He, K., Lin, S., Hopcroft, J.E.: Single image reflection removal through cascaded refinement. In: Proceedings of the IEEE/CVF Conference on Computer Vision and Pattern Recognition. pp. 3565–3574 (2020)
48. Li, R., Pan, J., Li, Z., Tang, J.: Single image dehazing via conditional generative adversarial network. In: Proceedings of the IEEE Conference on Computer Vision and Pattern Recognition. pp. 8202–8211 (2018)
49. Li, R., Tan, R.T., Cheong, L.F.: All in one bad weather removal using architectural search. In: Proceedings of the IEEE/CVF Conference on Computer Vision and Pattern Recognition. pp. 3175–3185 (2020)
50. Li, S., Araujo, I.B., Ren, W., Wang, Z., Tokuda, E.K., Junior, R.H., Cesar-Junior, R., Zhang, J., Guo, X., Cao, X.: Single image deraining: A comprehensive benchmark analysis. In: CVPR. pp. 3838–3847 (2019)
51. Li, W., Jafari, O.H., Rother, C.: Deep object co-segmentation. In: Asian Conference on Computer Vision. pp. 638–653. Springer (2018)

52. Li, X., Wu, J., Lin, Z., Liu, H., Zha, H.: Recurrent squeeze-and-excitation context aggregation net for single image deraining. In: Proceedings of the European Conference on Computer Vision (ECCV). pp. 254–269 (2018)
53. Lin, S., Ryabtsev, A., Sengupta, S., Curless, B.L., Seitz, S.M., Kemelmacher-Shlizerman, I.: Real-time high-resolution background matting. In: Proceedings of the IEEE/CVF Conference on Computer Vision and Pattern Recognition. pp. 8762–8771 (2021)
54. Liu, Y., Zhu, Z., Bai, X.: Wdnet: Watermark-decomposition network for visible watermark removal. In: Proceedings of the IEEE/CVF Winter Conference on Applications of Computer Vision. pp. 3685–3693 (2021)
55. Liu, Y.L., Lai, W.S., Yang, M.H., Chuang, Y.Y., Huang, J.B.: Learning to see through obstructions with layered decomposition. In: Proceedings of the IEEE Conference on Computer Vision and Pattern Recognition (2020)
56. Liu, Y.F., Jaw, D.W., Huang, S.C., Hwang, J.N.: Desnownet: Context-aware deep network for snow removal. IEEE Transactions on Image Processing **27**(6), 3064–3073 (2018)
57. Ma, D., Wan, R., Shi, B., Kot, A.C., Duan, L.Y.: Learning to jointly generate and separate reflections. In: Proceedings of the IEEE/CVF International Conference on Computer Vision. pp. 2444–2452 (2019)
58. Man, Z., Fu, X., Xiao, Z., Yang, G., Liu, A., Xiong, Z.: Unfolding taylor's approximations for image restoration. Advances in Neural Information Processing Systems **34**, 18997–19009 (2021)
59. Mao, X., Li, Q., Xie, H., Lau, R.Y., Wang, Z., Paul Smolley, S.: Least squares generative adversarial networks. In: IEEE international conference on computer vision (ICCV). pp. 2794–2802 (2017)
60. Mittal, A., Moorthy, A.K., Bovik, A.C.: No-reference image quality assessment in the spatial domain. IEEE Transactions on image processing **21**(12), 4695–4708 (2012)
61. Mittal, A., Soundararajan, R., Bovik, A.C.: Making a "completely blind" image quality analyzer. IEEE Signal processing letters **20**(3), 209–212 (2012)
62. Nayar, S.K., Narasimhan, S.G.: Vision in bad weather. In: Proceedings of the Seventh IEEE International Conference on Computer Vision. vol. 2, pp. 820–827. IEEE (1999)
63. Nilsback, M.E., Zisserman, A.: A visual vocabulary for flower classification. In: 2006 IEEE Computer Society Conference on Computer Vision and Pattern Recognition (CVPR'06). vol. 2, pp. 1447–1454. IEEE (2006)
64. Oliveira, P.R., Romero, R.A.: Improvements on ica mixture models for image preprocessing and segmentation. Neurocomputing **71**(10-12), 2180–2193 (2008)
65. Porav, H., Bruls, T., Newman, P.: I can see clearly now: Image restoration via deraining. In: 2019 International Conference on Robotics and Automation (ICRA). pp. 7087–7093. IEEE (2019)
66. Qian, R., Tan, R.T., Yang, W., Su, J., Liu, J.: Attentive generative adversarial network for raindrop removal from a single image. In: CVPR. pp. 2482–2491 (2018)
67. Qu, L., Tian, J., He, S., Tang, Y., Lau, R.W.: Deshadownet: A multi-context embedding deep network for shadow removal. In: Proceedings of the IEEE Conference on Computer Vision and Pattern Recognition. pp. 4067–4075 (2017)
68. Quan, R., Yu, X., Liang, Y., Yang, Y.: Removing raindrops and rain streaks in one go. In: Proceedings of the IEEE/CVF Conference on Computer Vision and Pattern Recognition. pp. 9147–9156 (2021)

69. Ren, W., Tian, J., Han, Z., Chan, A., Tang, Y.: Video desnowing and deraining based on matrix decomposition. In: Proceedings of the IEEE Conference on Computer Vision and Pattern Recognition. pp. 4210–4219 (2017)
70. Rother, C., Kolmogorov, V., Blake, A.: ” grabcut” interactive foreground extraction using iterated graph cuts. ACM transactions on graphics (TOG) **23**(3), 309–314 (2004)
71. Sakaridis, C., Dai, D., Van Gool, L.: Semantic foggy scene understanding with synthetic data. International Journal of Computer Vision **126**(9), 973–992 (2018)
72. Simonyan, K., Zisserman, A.: Very deep convolutional networks for large-scale image recognition. arXiv preprint arXiv:1409.1556 (2014)
73. Tan, R.T.: Visibility in bad weather from a single image. In: 2008 IEEE Conference on Computer Vision and Pattern Recognition. pp. 1–8. IEEE (2008)
74. Ulyanov, D., Vedaldi, A., Lempitsky, V.: Instance normalization: The missing ingredient for fast stylization. arXiv preprint arXiv:1607.08022 (2016)
75. Ulyanov, D., Vedaldi, A., Lempitsky, V.: Deep image prior. In: Proceedings of the IEEE conference on computer vision and pattern recognition. pp. 9446–9454 (2018)
76. Wang, H., Xie, Q., Zhao, Q., Meng, D.: A model-driven deep neural network for single image rain removal. In: Proceedings of the IEEE/CVF Conference on Computer Vision and Pattern Recognition. pp. 3103–3112 (2020)
77. Wang, J., Li, X., Yang, J.: Stacked conditional generative adversarial networks for jointly learning shadow detection and shadow removal. In: Proceedings of the IEEE Conference on Computer Vision and Pattern Recognition. pp. 1788–1797 (2018)
78. Wang, Z., Philion, J., Fidler, S., Kautz, J.: Learning indoor inverse rendering with 3d spatially-varying lighting. In: Proceedings of the IEEE/CVF International Conference on Computer Vision. pp. 12538–12547 (2021)
79. Wu, Y., He, Q., Xue, T., Garg, R., Chen, J., Veeraraghavan, A., Barron, J.T.: How to train neural networks for flare removal. Proceedings of the IEEE/CVF International Conference on Computer Vision (2021)
80. Xiao, J., Zhou, M., Fu, X., Liu, A., Zha, Z.J.: Improving de-raining generalization via neural reorganization. In: Proceedings of the IEEE/CVF International Conference on Computer Vision. pp. 4987–4996 (2021)
81. Xue, T., Rubinstein, M., Liu, C., Freeman, W.T.: A computational approach for obstruction-free photography. ACM Transactions on Graphics (TOG) **34**(4), 1–11 (2015)
82. Yang, Q., Tan, K.H., Ahuja, N.: Shadow removal using bilateral filtering. IEEE Transactions on Image processing **21**(10), 4361–4368 (2012)
83. Yang, W., Tan, R.T., Feng, J., Liu, J., Guo, Z., Yan, S.: Deep joint rain detection and removal from a single image. In: 2017 IEEE Conference on Computer Vision and Pattern Recognition (CVPR). pp. 1685–1694 (2017). https://doi.org/10.1109/CVPR.2017.183
84. Zamir, S.W., Arora, A., Khan, S., Hayat, M., Khan, F.S., Yang, M.H.: Restormer: Efficient transformer for high-resolution image restoration. CVPR (2022)
85. Zamir, S.W., Arora, A., Khan, S., Hayat, M., Khan, F.S., Yang, M.H., Shao, L.: Multi-stage progressive image restoration. In: CVPR (2021)
86. Zhang, H., Goodfellow, I., Metaxas, D., Odena, A.: Self-attention generative adversarial networks. In: International conference on machine learning. pp. 7354–7363. PMLR (2019)
87. Zhang, H., Sindagi, V., Patel, V.M.: Image de-raining using a conditional generative adversarial network. IEEE transactions on circuits and systems for video technology **30**(11), 3943–3956 (2019)

88. Zhang, K., Li, D., Luo, W., Ren, W., Liu, W.: Enhanced spatio-temporal interaction learning for video deraining: A faster and better framework. IEEE Transactions on Pattern Analysis and Machine Intelligence (2022)
89. Zhang, K., Li, D., Luo, W., Ren, W., Ma, L., Li, H.: Dual attention-in-attention model for joint rain streak and raindrop removal. arXiv preprint arXiv:2103.07051 (2021)
90. Zhang, K., Luo, W., Ren, W., Wang, J., Zhao, F., Ma, L., Li, H.: Beyond monocular deraining: Stereo image deraining via semantic understanding. In: European Conference on Computer Vision. pp. 71–89. Springer (2020)
91. Zhang, K., Luo, W., Yu, Y., Ren, W., Zhao, F., Li, C., Ma, L., Liu, W., Li, H.: Beyond monocular deraining: Parallel stereo deraining network via semantic prior. International Journal of Computer Vision pp. 1–16 (2022)
92. Zhang, X., Ng, R., Chen, Q.: Single image reflection separation with perceptual losses. In: Proceedings of the IEEE/CVF conference on computer vision and pattern recognition. pp. 4786–4794 (2018)
93. Zhong, Y., Dai, Y., Li, H.: Stereo computation for a single mixture image. In: Proceedings of the European Conference on Computer Vision (ECCV). pp. 435–450 (2018)
94. Zhou, M., Wang, F., Wei, X., Wang, R., Wang, X.: Pid controller-inspired model design for single image de-raining. IEEE Transactions on Circuits and Systems II: Express Briefs **69**(4), 2351–2355 (2021)
95. Zhou, M., Wang, R.: Control theory-inspired model design for single image de-raining. IEEE Transactions on Circuits and Systems II: Express Briefs **69**(2), 649–653 (2021)
96. Zhou, M., Xiao, J., Chang, Y., Fu, X., Liu, A., Pan, J., Zha, Z.J.: Image de-raining via continual learning. In: Proceedings of the IEEE/CVF Conference on Computer Vision and Pattern Recognition. pp. 4907–4916 (2021)
97. Zhou Wang, Bovik, A.C., Sheikh, H.R., Simoncelli, E.P.: Image quality assessment: from error visibility to structural similarity. IEEE Transactions on Image Processing **13**(4), 600–612 (2004). https://doi.org/10.1109/TIP.2003.819861
98. Zhu, J.Y., Park, T., Isola, P., Efros, A.A.: Unpaired image-to-image translation using cycle-consistent adversarial networks. In: Proceedings of the IEEE international conference on computer vision. pp. 2223–2232 (2017)
99. Zou, Z., Lei, S., Shi, T., Shi, Z., Ye, J.: Deep adversarial decomposition: A unified framework for separating superimposed images. In: Proceedings of the IEEE/CVF Conference on Computer Vision and Pattern Recognition. pp. 12806–12816 (2020)

A   Implementation Details

A.1   Training details, running time, and model size

BIDeN. We train BIDeN using a Tesla P100-PCIE-16GB GPU. The GPU driver version is 440.64.00 and the CUDA version is 10.2. We initialize weights using Xavier initialization [24]. For Task I (Mixed image decomposition across multiple domains), BIDeN (2) to BIDeN (8) takes approximately 37 hours, 50 hours, 61 hours, 71 hours, 82 hours, 91 hours, and 101 hours training time. For Task II.A (Real-scenario deraining in driving), the runtime of BIDeN is approximately 96 hours. However, BIDeN is required to perform additional mask reconstruction and source prediction tasks. By removing additional tasks from the training of BIDeN, the GPU hours can drop to 45 hours.

Double-DIP. We follow the default training setting of Double-DIP [23]. We use the official PyTorch implementation (link). We train a single image for 8000 iterations on a Tesla P100-PCIE-16GB GPU, the GPU driver version is 415.27 and the CUDA version is 10.0. The runtime for a single input image is approximately 20 minutes.

DAD. We follow the default training setting (Epoch 200, batch size 2, image crop size 256) of DAD [99]. Experiments are based on the official PyTorch implementation (link). We train DAD on a Tesla P100-PCIE-16GB GPU. The GPU driver version is 440.64.00 and the CUDA version is 10.2. DAD takes 13 hours of runtime.

MPRNet. We follow the default training setting (Epoch 250, batch size 16, image crop size 256) of MPRNet [85]. For a fair comparison, we apply the same data augmentation operations of BIDeN to MPRNet. We use the official PyTorch implementation (link) of MPRNet. We train MPRNet using 4 Tesla P100-PCIE-16GB GPU, the GPU driver version is 415.27 and the CUDA version is 10.0. The runtime of MPRNet is 20 hours and the model size of MPRNet is 41.8 MB.

Restormer. We follow the training setting used in link. Similar to MPRNet, we apply the same data augmentation operations used in BIDeN to Restormer. We reproduce our results based on a PyTorch implementation (link) of Restormer [84]. We train Restormer using a GeForce RTX 3900 GPU, the GPU driver version is 510.47 and the CUDA version is 11.6. The runtime of Restormer is approximately 8 hours and the model size is 25.3 MB.

A.2   Architecture of BIDeN

Following the naming convention used in CycleGAN [98] and perceptual loss [40], let **c3s1-k** denote a 3×3 Convolution-InstanceNorm-ReLU layer with stride 1 and k filters. **Rk** denotes a residual block that contains two 3×3 convolutional layers with the same number of filters on both layer and **Rk9** denotes nine continuous residual blocks. **uk** denotes a 3×3 fractional-strided-Convolution-InstanceNorm-ReLU layer with k filters and stride $\frac{1}{2}$. Let **Ck** denotes a 4×4 Convolution-InstanceNorm-LeakyReLU (slope 0.2) layer with k filters and stride 2. Both reflection padding and zero padding are employed.

Encoder. Our multi-scale encoder E contains three branches, we name them E_{B1}, E_{B2} and E_{B3}.

E_{B1} consists of c3s2-256, Rk9, c1s1-128. E_{B2} consists of c7s1-64, c3s2-128, c3s2-256, Rk9. E_{B3} contains c15s1-64, c3s2-128, c3s2-256, c3s1-256, c3s1-256, Rk9, c1s1-128. The number of parameters is 33.908 million for the encoder.

Heads. The architecture of each head H is: c1s1-256, c1s1-256, u128, u64, c7s1-3. Each head has 0.575 million parameters.

Discriminator. The discriminator D contains two branches, D_S (Separation) and D_P (Prediction). Most weights are shared, the shared part includes C64, C128, C256.

The last layer of D_S is C512. D_P contains c1s1-512 (LeakyReLu with slope 0.2), global max pooling, c1s1-N, where N is the maximum number of source components. The Discriminator has approximately 3.028 million parameters in total. The confidence threshold of D_P is 0.

A.3   Tasks

Task I: Mixed image decomposition across multiple domains. We use linear mix as the mixing mechanism. We do not introduce additional non-balanced mixing factors or non-linear mixing as Task I is challenging enough. The mixed image z is expressed as $z = \frac{1}{L} \sum_{j=1}^{L} x_{I_j}$. The possibilities of every component to be selected vary with the maximum number of source components N. We set the possibilities to be 0.9, 0.8, 0.7, 0.6, 0.5, 0.5, 0.5 for $N = 2, 3, 4, 5, 6, 7, 8$, respectively. As the mixing is linear, the order of mixing does not matter.

Task II: Real-scenario deraining. For both Task II.A and Task II.B, the mixing mechanism is based on the physical imaging models [83,56,32,10,65] and Koschmieder's law. The model for rain streak and snow is:

$I(x) = J(x)(1 - m(x)) + A * m(x),$

and the model for haze is:

$I(x) = J(x)t(x) + A(1 - t(x)),$

where x is the pixel of images, I is the observed intensity, J is the scene radiance, A is the global atmospheric light, and m is the mask of rain streak and snow. t denotes the transmission map. We set A between $[0.8, 1.0]$ during training, and fix $A = 0.9$ at test time.

To render the raindrop effect, we define a statistical model to estimate the location and motion of the raindrops. We employ the meta-ball model [6] for the interaction effect between multiple raindrops.

For raindrop positions, we randomly sample it over the entire scene. The raindrop radius is also randomly sampled. A single raindrop is combined with another 1 to 3 smaller raindrops to form a realistic raindrop shape. Each composite raindrop could further merge with other raindrops on the scene. The velocity along the y-axis of the raindrop is proportional to the raindrop radius. Raindrop masks are randomly selected on the time dimension for diversity. A simple refractive model [10] is employed. We create a look-up table T with three dimensions. The red and green channels together encode the texture of the raindrop, and the blue channel represents the thickness of the raindrops. Then, the

texture table T is masked by the alpha mask created by the meta-ball model. The masked table is dubbed M. The location (x,y) of the world point that is rendered at image location (u, v) on the surface of a raindrop is modeled as:

$x = u + (R_{(u,v)} * B_{(u,v)})$, $y = v + (G_{(u,v)} * B_{(u,v)})$.

where $R_{(u,v)}$, $B_{(u,v)}$ denote the pixel at location (u, v) in the red and blue channels of M.

We acquire the destination pixel coordinate for location (u,v) based on the above equations and generate the distorted image. We also apply random light reduction and blur to the distorted image. For the reduction, we set the rate r between $[0.8, 0.98]$ during training, and fix rate $r = 0.9$ at test time. The reduction can be expressed as $D = rD$, where D is the distorted image and r is the rate. We use a kernel size of 3 for Gaussian blur.

At last, we merge the distorted image with the original image:

$I(x) = \alpha(x)O(x) + (1 - \alpha(x)) * D(x)$,

where x denotes the pixel of images, I is the observed intensity, O is the original image, D is the distorted image, α is the value of the raindrop mask generated by the metaball model.

The probabilities of every component to be selected are 1.0, 0.5, 0.5, 0.5 for rain streak, snow, haze, and raindrop for Task II.A. The mixing order is rain streak, snow, haze, and raindrop. We design this since 1: streak and snow do not change the atmosphere a lot, so they should come first and 2: raindrops usually occur on the top of glass lens and are observed at first, thus they should come last. In Task II.B, the probabilities of every component to be selected are 0.6, 0.5, 0.5 for rain streak, snow, and raindrop. The mixing order is rain streak $\rightarrow$ snow $\rightarrow$ raindrop.

Task III: Joint shadow/reflection/watermark removal. We use paired shadow masks, shadow images, and shadow-free images provided in ISTD [77] and SRD [67,12]. The original SRD does not offer shadow masks, we use the shadow masks generated by Cun *et al.* [12].

The algorithm of adding reflection to images [92] is expressed as:

$I(x) = T(x) + R(x) * V(x)$,

where x is the pixel of images, I is the observed intensity, T is the transmission layer, R is the reflection layer, and V denotes the vignette mask. The reflection image R is processed by a Gaussian smoothing kernel with a random kernel size, where the size is in the range of 3 to 17 pixels during training, and fixed to 11 pixels during testing.

For watermarks, we follow the watermark composition model [54]. We use the RGB watermark images to add the watermark effect. We require the BID method to reconstruct the watermark mask. The watermark composition model is:

$I(x) = J(x)(1 - w(x)) + A * w(x)$,

where x denotes the pixel of images, I is the observed intensity, J is the scene radiance, A is the global atmospheric light, and w is the watermark image. We set A between $[0.8, 1.0]$ during training, and fix $A = 0.9$ for testing.

The probabilities of every component to be selected are 0.6, 0.5, 0.5 for shadow, reflection, and watermark, respectively. The order of mixing is shadow $\rightarrow$ reflection $\rightarrow$ watermark, as watermarks are usually added during post-processing

B   Additional Results

B.1   Additional results of Task I

Detailed case results of BIDeN. When the maximum number of components N increases, the number of possible z increases rapidly. There are $2^N - 1$ possible combinations between source components, that is, $2^N - 1$ cases. We present the detailed case results of BIDeN on Task I. We show the results of $N = 2, 3, 4, 5, 6$ (BIDeN (2), BIDeN (3), BIDeN (4), BIDeN (5), BIDeN (6)) in Table 7, Table 8, Table 9, Table 10, and Table 11. These results are the extensions of Table 1 in the main paper. Note that due to the difference in precision, the PSNR results reported here are slightly different (less than 0.5% difference) from the PSNR results reported in the main paper.

Qualitative results of BIDeN. Here we present more qualitative results of BIDeN. We show the results of $N = 2, 3, 4, 5, 6$ (BIDeN (2), BIDeN (3), BIDeN (4), BIDeN (5), BIDeN (6)) in Figure 8, Figure 9, Figure 10, Figure 11, and Figure 12. The number of selected source components L and the index set I are randomly chosen. The eight source components in Task I are Fruit (A), Animal (B), Flower (C), Furniture (D), Yosemite (E), Vehicle (F), Vegetable (G), and CityScape (H).

Table 7. Detailed case results of BIDeN (2) on Task I (Mixed image decomposition across multiple domains)

Input	A	B	Acc
a	25.26	-	0.940
b	-	25.11	0.933
ab	20.09	19.93	1.000

Table 8. Detailed case results of BIDeN (3) on Task I (Mixed image decomposition across multiple domains)

Input	A	B	C	Acc
a	24.04	-	-	0.906
b	-	23.48	-	0.953
c	-	-	22.74	0.756
ab	19.07	18.78	-	0.833
ac	18.96	-	18.27	0.573
bc	-	18.31	18.25	0.763
Avg	19.01	18.54	18.26	0.723
abc	16.66	15.89	16.27	0.983

Table 9. Detailed case results of BIDeN (4) on Task I (Mixed image decomposition across multiple domains)

Input	A	B	C	D	Acc
a	23.07	-	-	-	0.896
b	-	22.61	-	-	0.886
c	-	-	21.93	-	0.770
d	-	-	-	21.88	0.933
ab	18.22	18.06	-	-	0.710
ac	18.20	-	17.41	-	0.560
ad	18.85	-	-	18.51	0.783
bc	-	16.98	17.56	-	0.710
bd	-	18.06	-	17.79	0.856
cd	-	-	18.44	18.77	0.656
Avg	18.42	17.7	17.80	18.35	0.712
abc	16.12	15.46	15.70	-	0.660
abd	16.47	15.95	-	16.40	0.676
acd	16.36	-	16.11	16.78	0.396
bcd	-	15.63	16.52	16.52	0.563
Avg	18.42	17.7	17.80	18.35	0.712
abcd	15.11	14.37	14.98	15.43	0.943

Table 10. Detailed case results of BIDeN (5) on Task I (Mixed image decomposition across multiple domains)

Input	A	B	C	D	E	Acc
a	22.75	-	-	-	-	0.840
b	-	22.02	-	-	-	0.853
c	-	-	22.30	-	-	0.553
d	-	-	-	22.52	-	0.930
e	-	-	-	-	20.77	0.923
ab	17.68	17.30	-	-	-	0.676
ac	17.60	-	17.19	-	-	0.373
ad	18.34	-	-	18.26	-	0.720
ae	18.94	-	-	-	18.36	0.700
bc	-	16.98	17.56	-	-	0.633
bd	-	17.21	-	17.60	-	0.716
be	-	17.37	-	-	17.54	0.710
cd	-	-	18.42	18.72	-	0.443
ce	-	-	18.79	-	18.34	0.556
de	-	-	-	18.18	17.94	0.796
Avg	18.14	17.21	17.99	18.19	18.04	0.632
abc	15.72	14.92	15.62	-	-	0.570
abd	16.11	15.29	-	16.15	-	0.573
abe	16.38	15.12	-	-	16.32	0.526
acd	15.91	-	15.94	16.53	-	0.320
ace	16.27	-	16.07	-	16.80	0.266
ade	16.72	-	-	16.25	16.62	0.486
bcd	-	15.04	16.46	16.32	-	0.576
bce	-	14.94	16.62	-	16.38	0.553
bde	-	15.24	-	16.07	16.15	0.736
cde	-	-	17.08	16.48	16.52	0.366
Avg	16.18	15.09	16.29	16.30	16.46	0.497
abcd	14.82	13.91	14.94	15.11	-	0.633
abce	14.97	13.80	15.06	-	15.50	0.480
abde	15.20	14.14	-	14.99	15.32	0.586
acde	15.03	-	15.23	15.11	15.62	0.180
bcde	-	13.92	15.74	15.06	15.34	0.570
Avg	14.99	13.94	15.24	15.06	15.44	0.489
abcde	14.23	13.28	14.52	14.20	14.74	0.860

Table 11. Detailed case results of BIDeN (6) on Task I (Mixed image decomposition across multiple domains)

Input	A	B	C	D	E	F	Acc
a	22.82	-	-	-	-	-	0.850
b	-	21.80	-	-	-	-	0.826
c	-	-	22.61	-	-	-	0.823
d	-	-	-	22.50	-	-	0.890
e	-	-	-	-	21.09	-	0.910
f	-	-	-	-	-	21.97	0.893
ab	17.31	16.79	-	-	-	-	0.646
ac	17.10	-	16.84	-	-	-	0.526
ad	18.14	-	-	17.66	-	-	0.613
ae	18.59	-	-	-	18.24	-	0.676
af	18.24	-	-	-	-	17.76	0.583
bc	-	16.60	17.46	-	-	-	0.613
bd	-	16.95	-	17.05	-	-	0.593
be	-	16.81	-	-	17.30	-	0.660
bf	-	16.90	-	-	-	17.04	0.510
cd	-	-	18.23	18.11	-	-	0.480
ce	-	-	18.53	-	18.16	-	0.670
cf	-	-	18.13	-	-	17.48	0.583
de	-	-	-	17.43	17.86	-	0.653
df	-	-	-	16.18	-	16.01	0.686
ef	-	-	-	-	17.42	16.74	0.673
Avg	17.87	16.81	17.83	17.28	17.79	17.00	0.654
abc	15.29	14.56	15.34	-	-	-	0.606
abd	15.83	14.95	-	15.51	-	-	0.390
abe	16.10	14.59	-	-	16.04	-	0.513
abf	15.89	14.78	-	-	-	15.61	0.333
acd	15.49	-	15.56	15.98	-	-	0.313
ace	15.88	-	15.67	-	16.55	-	0.350
acf	15.64	-	15.46	-	-	15.61	0.303
ade	16.46	-	-	15.59	16.45	-	0.330
adf	16.15	-	-	14.60	-	14.73	0.450
aef	16.44	-	-	-	15.99	15.18	0.373
bce	-	14.68	16.24	15.71	-	-	0.370
bce	-	14.43	16.43	-	16.08	-	0.500
bcf	-	14.69	16.04	-	-	15.42	0.346
bde	-	14.90	-	15.45	15.89	-	0.516
bdf	-	14.87	-	14.60	-	14.52	0.456
bef	-	14.81	-	-	15.60	15.04	0.400
cde	-	-	16.82	15.84	16.30	-	0.253
cdf	-	-	16.48	14.86	-	14.59	0.383
cef	-	-	16.64	-	15.91	15.15	0.443
def	-	-	-	14.70	15.80	14.26	0.506
Avg	15.92	14.72	16.06	15.28	16.06	16.71	0.439
abcd	14.45	13.69	14.61	14.62	-	-	0.420
abce	14.63	13.51	14.76	-	15.20	-	0.540
abcf	14.57	13.65	14.54	-	-	14.34	0.313
abde	15.02	13.79	-	14.36	15.05	-	0.323
abdf	14.90	13.80	-	13.77	-	13.81	0.373
abef	15.13	13.70	-	-	14.77	14.17	0.276
acde	14.71	-	14.88	14.60	15.34	-	0.126
acdf	14.61	-	14.67	13.97	-	13.75	0.220
acef	14.80	-	14.81	-	14.99	14.14	0.193
adef	15.13	-	-	14.81	15.00	13.50	0.293
bcde	-	13.64	15.55	14.56	14.98	-	0.296
bcdf	-	13.76	15.26	13.96	-	13.66	0.336
bcef	-	13.63	15.35	-	14.84	14.10	0.356
bdef	-	13.86	-	13.78	14.74	13.49	0.543
cdef	-	-	15.62	13.99	14.99	13.44	0.206
Avg	14.79	13.70	15.00	14.24	14.99	13.84	0.321
abcde	13.97	13.12	14.24	13.73	14.41	-	0.350
abcdf	13.93	13.22	14.05	13.38	-	13.14	0.543
abcef	14.04	13.09	14.17	-	14.23	13.41	0.346
abedf	14.30	13.25	-	13.24	14.20	12.99	0.516
acdef	14.03	-	14.28	13.40	14.37	12.94	0.140
bcdef	-	13.18	14.76	13.40	14.19	12.92	0.356
Avg	14.04	13.17	14.30	13.43	14.28	13.08	0.375
abcdef	13.54	12.86	13.82	12.95	13.80	12.57	0.846

Input   Head (A)   Head (B)
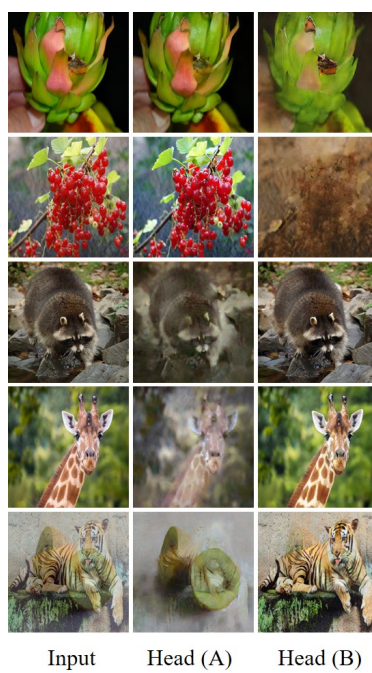
Fig. 8. Qualitative results of BIDeN (2). Fruit (A), Animal (B). Row 1-2: a. Row 3-4: b. Row 5: ab
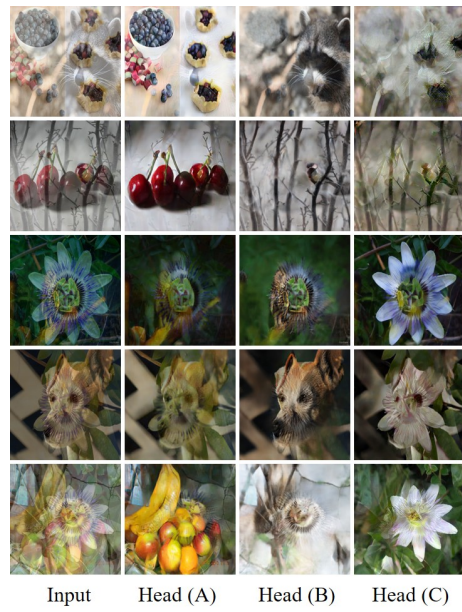
Fig. 9. Qualitative results of BIDeN (3). Fruit (A), Animal (B), Flower (C). Row 1-2: ab. Row 3-4: bc. Row 5: abc
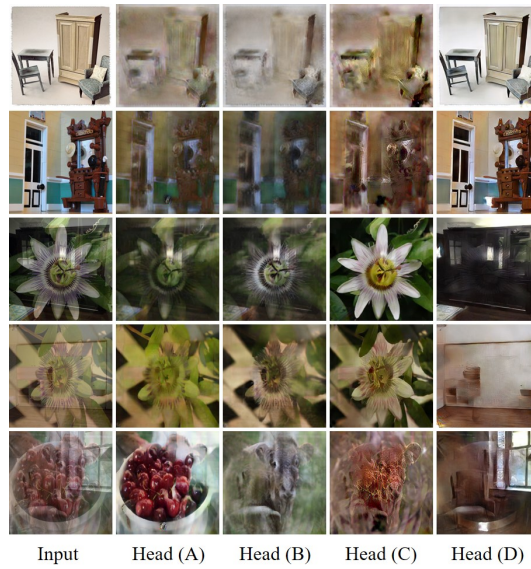

Fig. 10. Qualitative results of BIDeN (4). Fruit (A), Animal (B), Flower (C), Furniture (D). Row 1-2: d. Row 3-4: cd. Row 5: abd
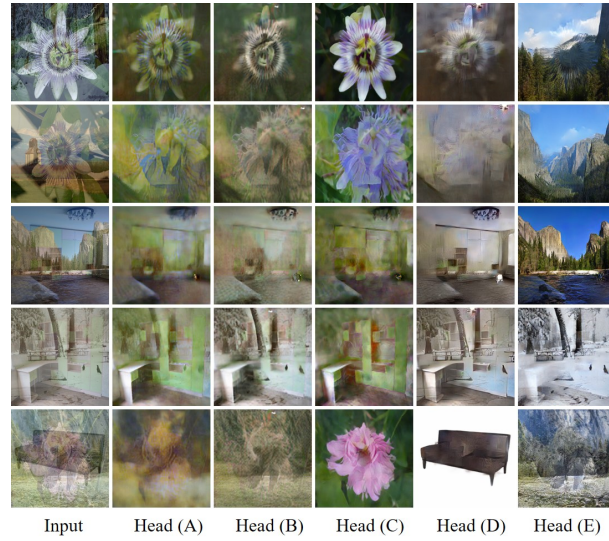
Fig. 11. Qualitative results of BIDeN (5). Fruit (A), Animal (B), Flower (C), Furniture (D), Yosemite (E). Row 1-2: ce. Row 3-4: de. Row 5: bcde
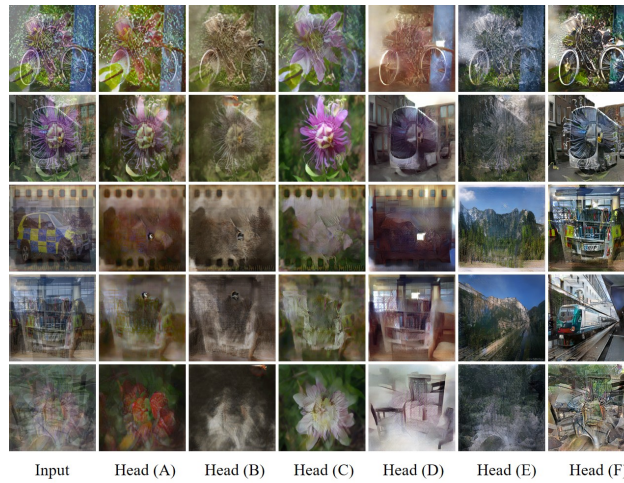

Fig. 12. Qualitative results of BIDeN (6). Fruit (A), Animal (B), Flower (C), Furniture (D), Yosemite (E), Vehicle (F). Row 1-2: cf. Row 3-4: def. Row 5: abcdef

B.2   Additional results of Task II

For Task II.A (Real-scenario deraining in driving), more qualitative results are provided. Visual examples of CityScapes/masks/transmission maps generated by BIDeN are shown in Figure 13. We present more qualitative comparisons between BIDeN and MPRNet [85] in Figure 14 and Figure 15. The comparison presents the results of 6 cases from the same scene.

For the default training setting on Task II.A, the probabilities of every component to be selected are 1.0, 0.5, 0.5, 0.5 for rain streak, snow, raindrop, and haze. Moreover, we train both BIDeN and MPRNet again setting the possibility of the rain streak component to be selected as 0.8. The quantitative results of BIDeN and the comparison between MPRNet are provided in Table 12 and Table 13. Compared to BIDeN trained under the default training setting of Task II.A, BIDeN performs better when the possibility of the rain streak component to be selected is set to 0.8.
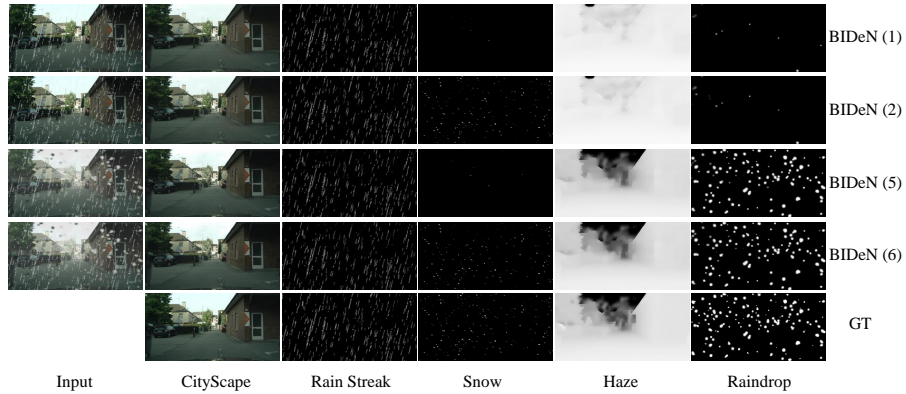

Fig. 13. CityScape, masks (Rain Streak, Snow, Raindrop), and transmission map (Haze) generated by BIDeN for case (1), case (2), case (5), and case (6). Case (1): rain streak, case (2): rain streak + snow, case (5): rain streak + moderate haze + raindrop, case (6): rain streak + snow + moderate haze + raindrop
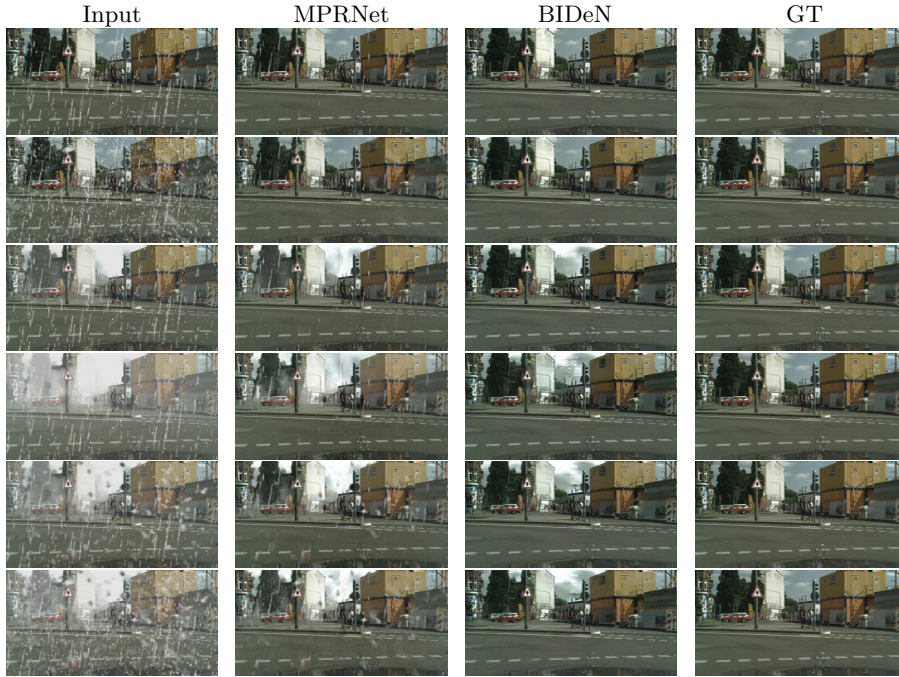
Fig. 14. Additional results of Task II.A (Real-scenario deraining in driving). Row 1-6 presents 6 cases of a same scene. The 6 cases are (1): rain streak, (2): rain streak + snow, (3): rain streak + light haze, (4): rain streak + heavy haze, (5): rain streak + moderate haze + raindrop, (6) rain streak + snow + moderate haze + raindrop. BIDeN remove all components of rain efficiently while MPRNet leaves some components that are not completely removed

Table 12. Results of BIDeN on Task II.A (Real-scenario deraining in driving). The possibility of the rain streak component to be selected is 0.8. We employ PSNR and SSIM metrics for both CityScape images, masks, and transmission maps. We report the results for 6 test cases as presented in Figure 1 of the main paper, the 6 cases are (1): rain streak, (2): rain streak + snow, (3): rain streak + light haze, (4): rain streak + heavy haze, (5): rain streak + moderate haze + raindrop, (6) rain streak + snow + moderate haze + raindrop. Note that only haze is divided into light/moderate/heavy intensities. Both training set and test set of Rain Streak, Snow, and Raindrop already consist of different intensities

Method	CityScape PSNR↑	SSIM↑	Rain Streak PSNR↑	SSIM↑	Snow PSNR↑	SSIM↑	Haze PSNR↑	SSIM↑	Raindrop PSNR↑	SSIM↑	Acc ↑
BIDeN (1)	33.30	0.930	31.55	0.917	-	-	-	-	-	-	1.0
BIDeN (2)	29.55	0.896	28.80	0.836	25.74	0.689	-	-	-	-	0.992
BIDeN (3)	29.38	0.919	30.98	0.907	-	-	31.11	0.956	-	-	0.994
BIDeN (4)	27.56	0.899	30.39	0.895	-	-	31.83	0.944	-	-	0.994
BIDeN (5)	27.89	0.900	30.17	0.891	-	-	30.73	0.945	22.32	0.904	0.996
BIDeN (6)	27.05	0.869	28.05	0.815	24.81	0.653	30.02	0.940	21.55	0.888	0.990

| Input	MPRNet	BIDeN	GT
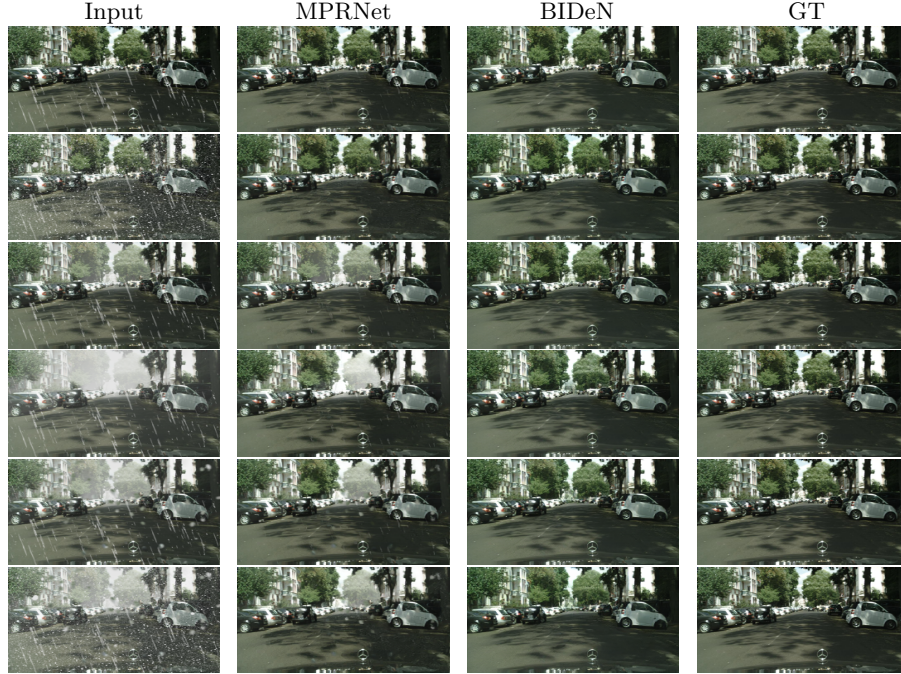
Fig. 15. Additional results of Task II.A (Real-scenario deraining in driving). Row 1-6 presents 6 cases of a same scene. The 6 cases are (1): rain streak, (2): rain streak + snow, (3): rain streak + light haze, (4): rain streak + heavy haze, (5): rain streak + moderate haze + raindrop, (6) rain streak + snow + moderate haze + raindrop. BIDeN remove all components of rain efficiently while MPRNet leaves some components that are not completely removed

Table 13. Comparison on Task II.A (Real-scenario deraining in driving) between BIDeN and MPRNet [85]. The possibility of the rain streak component to be selected is 0.8. MPRNet shows superior results for case (1) and case (2). In contrast, BIDeN is better at other cases. For the details of 6 test cases, please refer to Table 12 and Figure 1 of the main paper

Case	Input PSNR↑	SSIM↑	MPRNet PSNR↑	SSIM↑	BIDeN PSNR↑	SSIM↑
(1)	25.69	0.786	33.03	0.941	33.30	0.930
(2)	18.64	0.564	30.44	0.902	29.55	0.896
(3)	17.45	0.712	23.95	0.897	29.38	0.919
(4)	11.12	0.571	17.32	0.810	27.56	0.899
(5)	14.05	0.616	20.75	0.839	27.89	0.900
(6)	12.38	0.461	19.74	0.798	27.05	0.869

B.3   Additional results of Task III

For Task III (Joint shadow/reflection/watermark removal), Figure 16 presents the qualitative comparison between BIDeN and two state-of-the-art baselines [12,19]. Though suffering from a color shift, BIDeN still shows visually pleasing, ghost-free shadow removal results. We also provide additional results of BIDeN for all cases. Results of Version one (V1) and Version two (V2) are shown in Figure 17 and Figure 18.
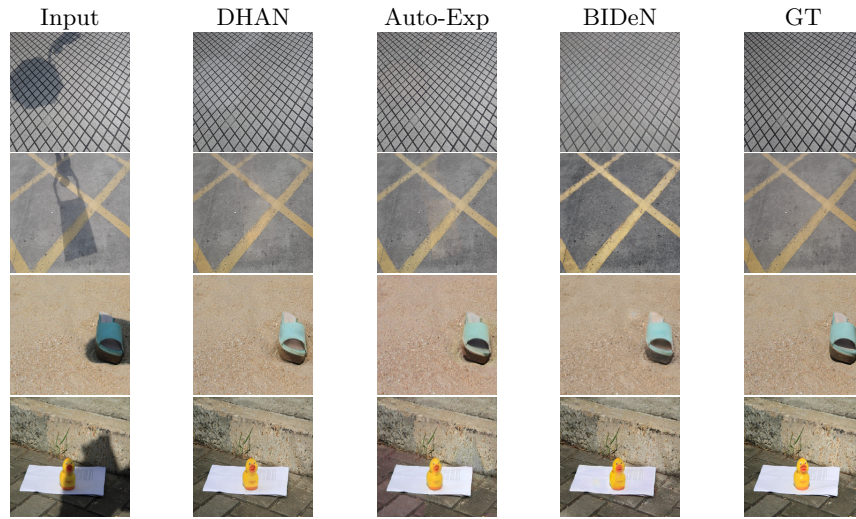
Fig. 16. Results of Task III (Joint shadow/reflection/watermark removal). Row 1-2 show the results of Version one (V1) and Row 3-4 present the results of Version two (V2). We compare BIDeN to DHAN [12] and Auto-Exposure [19] on shadow removal task. Though the performance of BIDeN is constrained by the generality of BIDeN and BID training setting, BIDeN still efficiently removes the shadow and shows competitive results. However, BIDeN suffers from a color shift whereas DHAN and Auto-Exposure better keep the fidelity of the original colors

|					
					a
					ab
					ac
					abc
					b
					c
					bc
					GT
Input	ISTD	Shadow(a)	Reflection(b)	Watermark(c)	
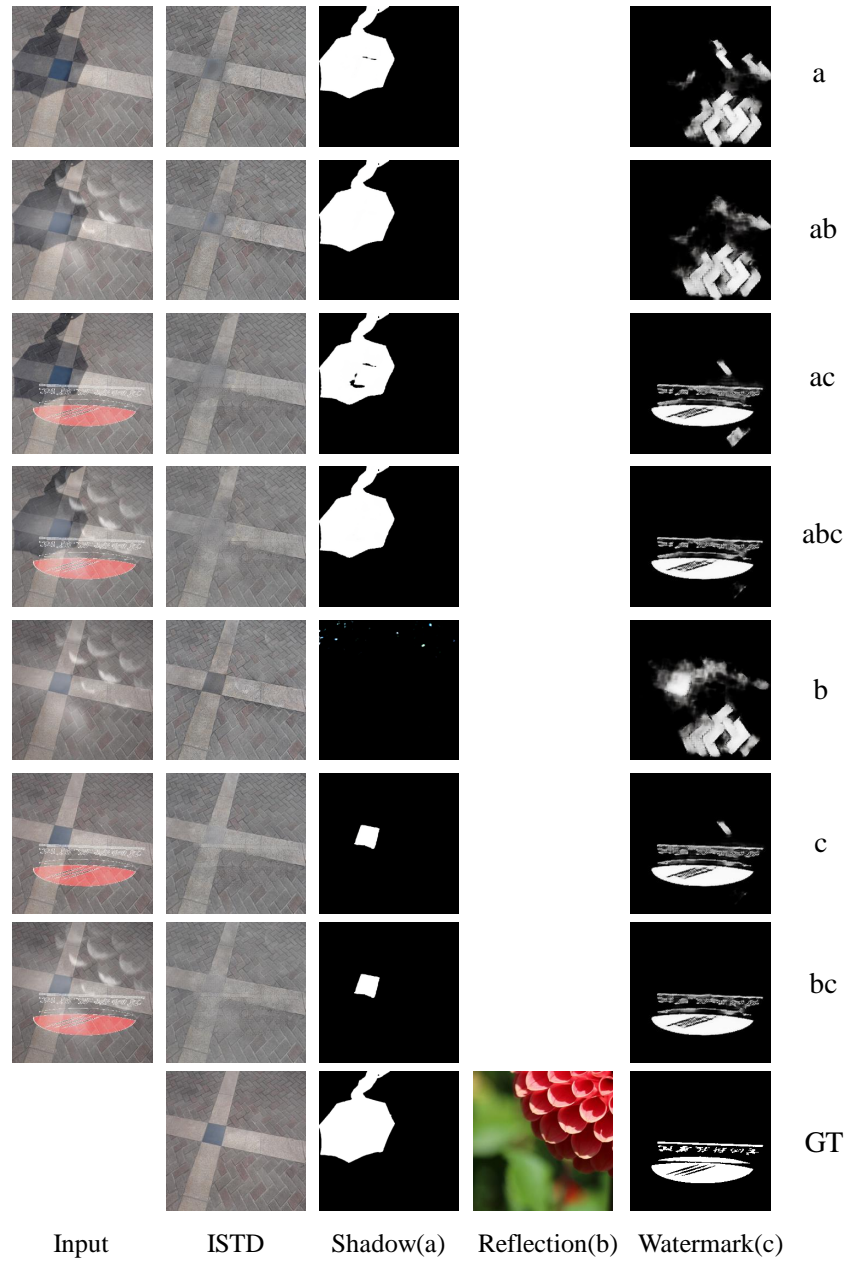
Fig. 17. All case results of Task III (Joint shadow/reflection/watermark removal), Version one (V1). ISTD images, shadow masks, and watermark masks generated by BIDeN for all cases. The order of all cases is identical to Table 4 of the main paper. The generated ISTD images suffer color shift, but all shadow/reflection/watermark are efficiently removed for all cases

					a
					ab
					ac
					abc
					b
					c
					bc
					GT
Input	ISTD	Shadow(a)	Reflection(b)	Watermark(c)	
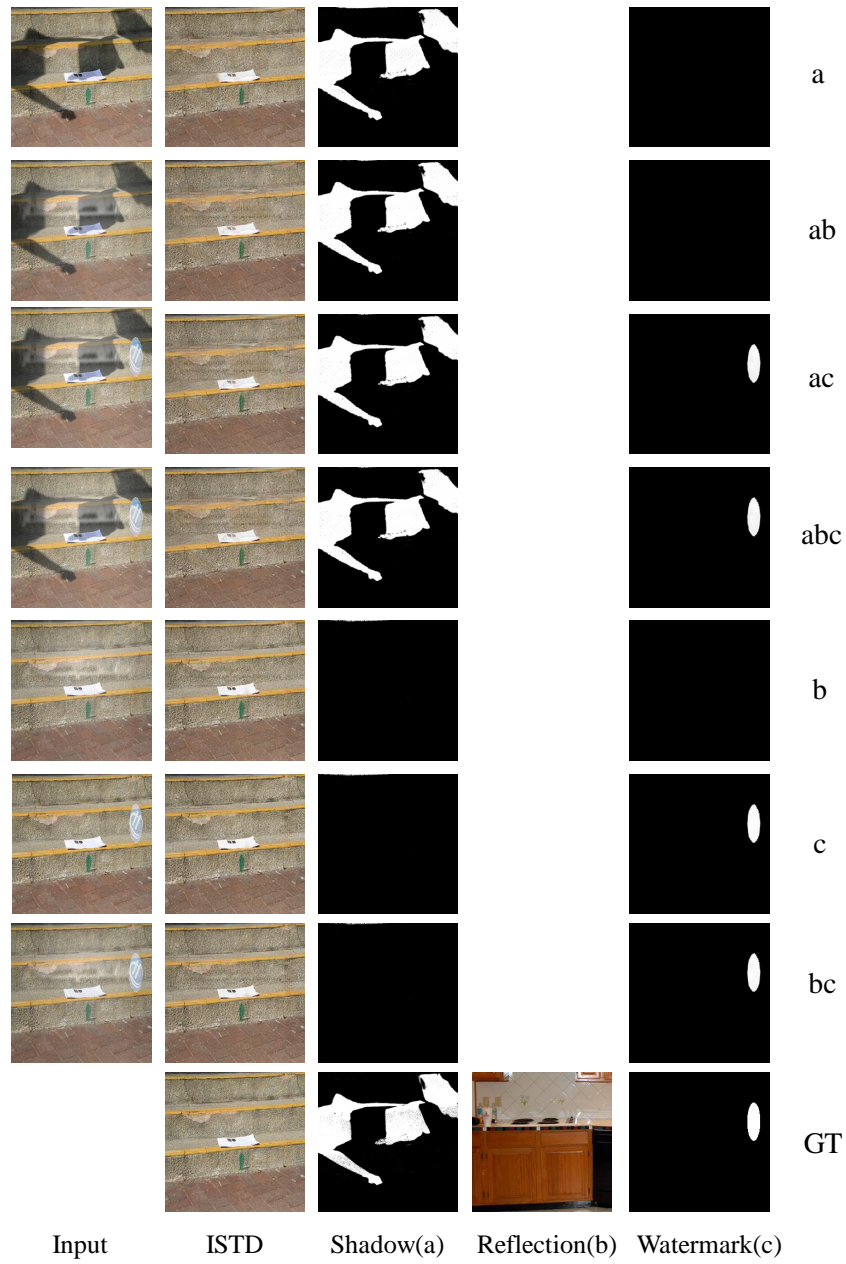
Fig. 18. All case results of Task III (Joint shadow/reflection/watermark removal), Version two (V2). ISTD images, shadow masks, and watermark masks generated by BIDeN for all cases. The order of all cases is identical to Table 4 of the main paper. All shadow/reflection/watermark are efficiently removed for all cases